JACS
JOURNAL OF THE AMERICAN CHEMICAL SOCIETY
pubs.acs.org/JACS
Article

Structure–Activity-Driven Multicompartment Lipid Nanoparticles for Synergistic mRNA and siRNA Codelivery in Acute Myeloid Leukemia

Xiaofei Xin,*,○ Yifu Lyu,○ Huanyu Qin,○ Jinyu Dai, Di Wu, Yu Ding, Qiang Tian, Chao Qin,* Na Li,* and Lifang Yin*

Cite This: https://doi.org/10.1021/jacs.5c23209
Read Online
ACCESS | Metrics & More | Article Recommendations | SI Supporting Information

ABSTRACT: The rational design of nonlamellar, multicompartment lipid nanoparticles (LNPs) offers a promising strategy for advancing nucleic acid delivery and immunotherapy. In this study, imidazole-based LNPs (A3-DM/DL-LNPs) with a mesoscopically disordered internal structure resembling the sponge phase were developed, enabling efficient codelivery of mRNA and STAT3-targeting siRNA (siSTAT3). Small-angle scattering analysis revealed a unique quasi-periodic arrangement in A3-DM/DL-LNPs, characterized by broader interdomain spacing and higher membrane heterogeneity compared to benchmark ALC-0315-LNPs, suggesting enhanced endocytosis efficiency and more favorable RNA encapsulation. The "M-shaped" polar headgroup, formed by a piperazine ring flanked by two imidazole moieties, promoted membrane interaction, cellular uptake, and transfection efficiency. In contrast, alternative LNPs with linear polar head structures (A3-SS/SM/SL-LNPs and A4-SS/SM/SL-LNPs) showed inferior delivery performance. Raman spectroscopy revealed that lipid spatial localization correlated with RNA expression in the spleen and lymph nodes, highlighting the importance of LNP structure in immune activation and targeting specific immune organs. Functionally, A3-DM/DL-LNPs restored dendritic cell (DC) antigen presentation, alleviated endoplasmic reticulum (ER) stress, and reversed T cell exhaustion in acute myeloid leukemia (AML), triggering strong immune responses and enhancing natural killer (NK) cell and T cell-mediated antileukemic activity, thereby improving therapeutic outcomes.

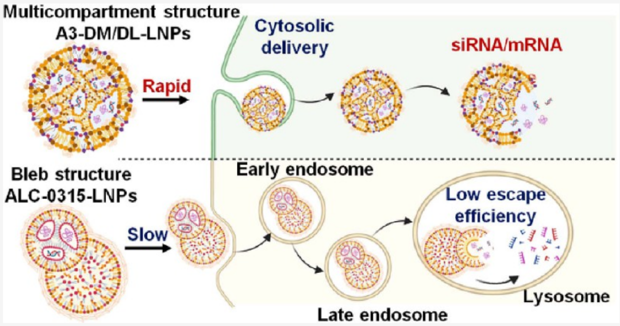

INTRODUCTION

Acute myeloid leukemia (AML) is a highly heterogeneous hematologic malignancy characterized by clonal proliferation of hematopoietic stem and progenitor cells, leading to bone marrow failure and extramedullary organ infiltration.[1−3] Despite major advances in immunotherapy for solid tumors and lymphoid malignancies, translating these successes to AML has proven particularly challenging due to profound genetic and clonal heterogeneity, the limited availability of leukemia-associated antigens with sufficient specificity and coverage, and a strongly immunosuppressive tumor microenvironment that limits effective antigen presentation and T-cell activation.[4,5] mRNA-based cancer vaccines have emerged as a promising strategy to address antigenic heterogeneity by enabling endogenous tumor antigen expression in antigen-presenting cells (APCs), thereby promoting antigen-specific T-cell responses and immunological memory.[6] In line with this concept, DC-based mRNA vaccines targeting leukemia-associated antigens such as human telomerase reverse transcriptase (hTERT) and Wilms' tumor 1 (WT1) have shown encouraging but heterogeneous clinical activity in AML. A phase I trial reported that 11 of 19 patients vaccinated with hTERT mRNA-loaded DCs remained disease-free at the latest follow-up,[7] and a phase II WT1 mRNA-DC study demonstrated a vaccine-induced relapse reduction rate of 25% with significantly improved 5-year relapse-free survival in responders compared with nonresponders (50% vs 7.7%).[8] These findings highlight both the therapeutic potential of mRNA vaccination and the presence of response-limiting mechanisms within the AML immune microenvironment. However, mounting evidence indicates that the heterogeneous efficacy of mRNA-based immunotherapy in AML is largely attributable to STAT3-driven DC dysfunction, resulting in impaired antigen presentation and immune suppression.[9−11] Accordingly, inhibition of STAT3 signaling has been shown to restore DC function, enhance cytotoxic T-cell responses, and reduce

Received: December 27, 2025
Revised: February 7, 2026
Accepted: February 10, 2026

Scheme 1. Schematic Illustration of Imidazole-based Bipolar Ionizable Lipid-Driven Multicompartment LNPs for Synergistic Codelivery of siSTAT3 and mRNA in AML Therapy[a]

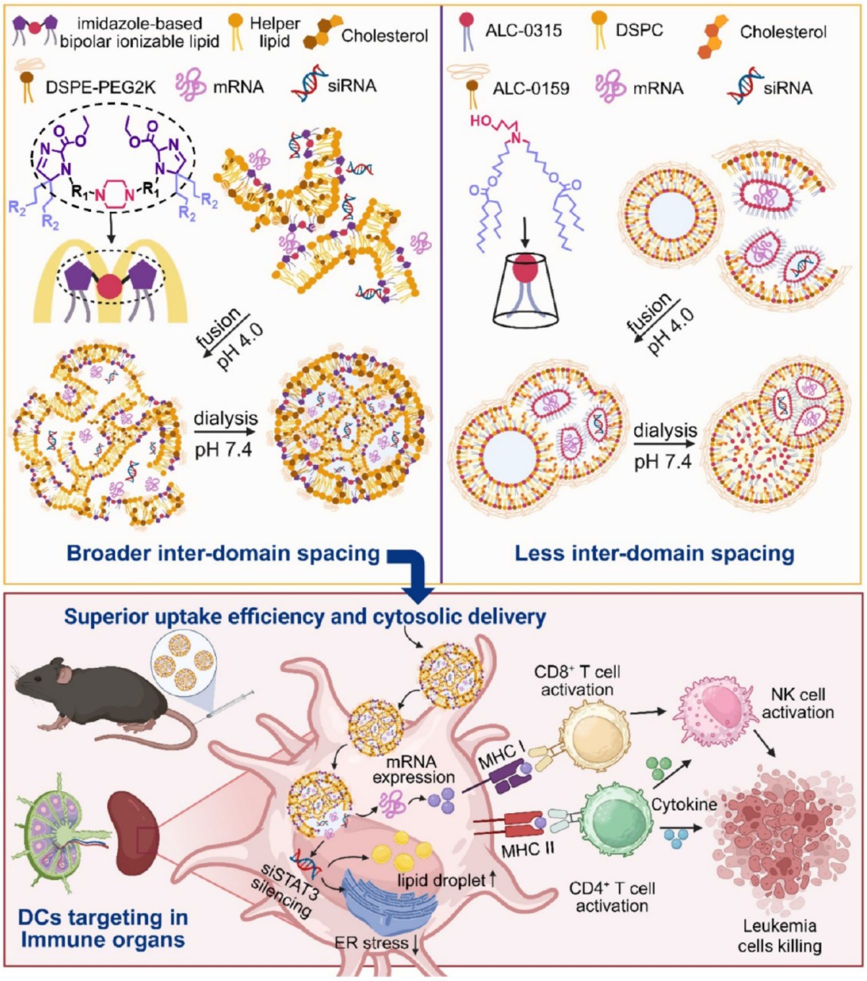

[a]M-shaped bipolar ionizable lipids assemble into irregular bilayer membranes under acidic conditions, creating enlarged interfacial areas that promote efficient encapsulation of both mRNA and siRNA. Subsequent membrane fusion generates multicompartment structures that are stabilized into spherical LNPs through dialysis. In contrast, benchmark ALC-0315 lipids preferentially form single-layered reversed micelles, encapsulating less RNA and eventually fusing into bleb-like LNPs. The resulting multicompartment LNPs codeliver mRNA and siSTAT3 to silence STAT3, alleviate ER stress, and modulate lipid droplet dynamics in dendritic cells, thereby enhancing antigen presentation. This process restores T cell immunity and elicits durable systemic antileukemic responses. The scheme was created using BioRender.com.

immunosuppressive cytokine production, including through clinically approved tyrosine kinase inhibitors and small-molecule STAT3 inhibitors.[12−18] Building on this rationale, RNA interference offers a precise approach to suppress STAT3 signaling, and codelivery of siSTAT3 with mRNA encoding tumor antigens has the potential to simultaneously enhance antigen presentation and reverse immune suppression, establishing a self-reinforcing immune circuit against AML.[19−22]

Due to the distinct molecular characteristics between rigid, short-chain siRNA (<30 nucleotides) and large, highly structured mRNA molecules (>103 nucleotides), benchmark lipid nanoparticle (LNP) formulations using ionizable lipids such as DLin-MC3-DMA (MC3) and ALC-0315 exhibit pronounced nanoheterogeneity. Specifically, LNP-siRNA systems tend to form tightly packed multilamellar structures, while LNP-mRNA formulations display bleb-like bilayer morphologies.[23,24] These differences are further exacerbated during the rapid mixing step of microfluidic-based LNP production, where strong electrostatic repulsion between densely packed, negatively charged RNA chains complicates the coassembly of siRNA and mRNA within a single nanoparticle formulation.[25−28] Mechanistically, LNPs function as soft-matter nanoscale assemblies, whose internal architecture is primarily governed by the structural preferences and interactions among ionizable lipid, cholesterol and helper lipids, allowing them to accommodate the divergent physical properties of mRNA and siRNA.[29−31] Recent studies indicate that nonlamellar LNP structures can significantly enhance the coencapsulation of both RNA types by promoting membrane homeostasis and maintaining high transfection efficiency, even under extreme environmental conditions such as elevated temperature and pressure.[32−35] Collectively, these findings highlight the importance of a bottom-up, chemistry-driven rational design of ionizable lipids, guided by a deep understanding of structure−activity relationships, to develop next-generation LNPs capable of efficiently codelivering mRNA and siRNA.

Here, we present a series of multicompartment LNPs formulated with imidazole-derived ionizable lipids, inspired by

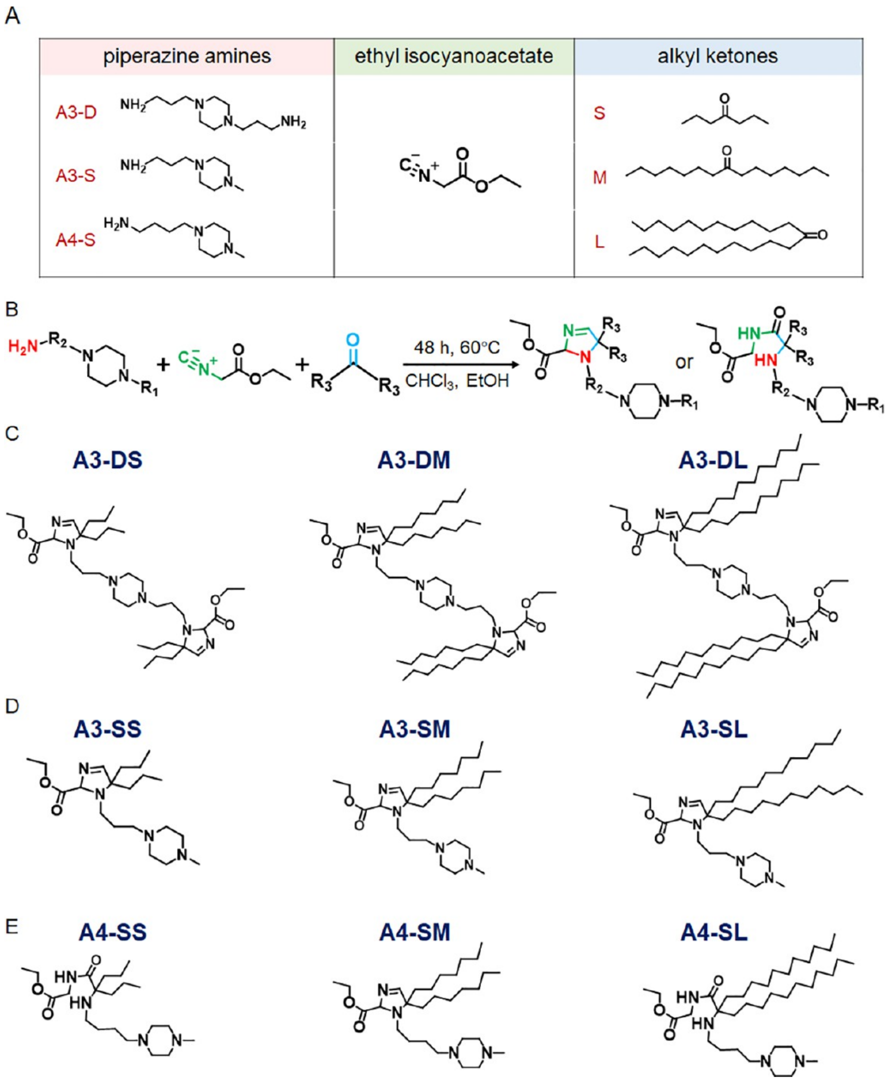

Figure 1. Synthesis of imidazole-based ionizable lipids. (**A**) The combinatorial lipid library is constructed from a three-component architecture comprising piperazine amines, ethyl isocyanoacetate, and alkyl ketones. (**B**) Schematic illustration of the synthetic route for the designed lipids. R1 denotes the substituent on the piperazine nitrogen and adopts two defined configurations in this library: a methyl group for single-tailed lipids (A3-S and A4-S), and a piperazine-linked moiety identical to that on the opposite side for the double-tailed A3-D series, resulting in a symmetric bipolar architecture. R2 denotes the carbon chain length of the piperazine linker, which is 3, 3, and 4 for A3-D, A3-S, and A4-S, respectively. R3 denotes the carbon chain length of the hydrophobic tail, with values of 3 (S), 7 (M), and 11 (L). (**C**−**E**) Chemical structures of the imidazole-based bipolar ionizable lipids. This modular design enables systematic evaluation of structure−activity relationships across lipid architectures.

the inverted conical lipid components found in eukaryotic and bacterial membranes, using a molecular hybridization strategy. To comprehensively evaluate the physical and interfacial properties of these LNPs, we employed cryogenic transmission electron microscopy (cryo-TEM), small-angle X-ray scattering (SAXS), and atomic force microscopy (AFM). The resulting multicompartment LNPs exhibited dynamic aggregation with other formulation components and preferentially associated with RNA molecules, giving rise to nonlamellar phases characterized by both disordered and periodic structures within the particle core. This unique topology demonstrated high thermal stability and enabled efficient encapsulation of structurally diverse RNA therapeutics, supporting enhanced cytosolic delivery through improved affinity for cellular membranes. Notably, these LNPs exhibited preferential accumulation in the spleen and lymph nodes, with selective targeting of myeloid cells. Delivery of siRNA targeting STAT3 (siSTAT3) promoted DC cross-presentation by modulating endoplasmic reticulum (ER) stress and inducing lipid droplet formation, which in turn facilitated stable antigen presentation from codelivered mRNA, thereby redirecting T cell responses and sustaining antileukemic immunity in AML. Altogether, our imidazole-based bipolar ionizable lipid-derived LNP platform offers a promising approach for the codelivery of mRNA and siRNA, opening new avenues for enhancing the efficacy of RNA therapeutics in AML treatment (Scheme 1).

■ RESULTS

Design and Synthesis of Imidazole-Based Bipolar Ionizable Lipids

Inspired by the spontaneous formation of hexagonal-phase lipid packing observed in cardiolipin and monoglucosyl diacylglyceride, key components of asymmetric bacterial membranes, we hypothesized that lipid species featuring bulky polar head groups, cyclic configurations, and multiacyl

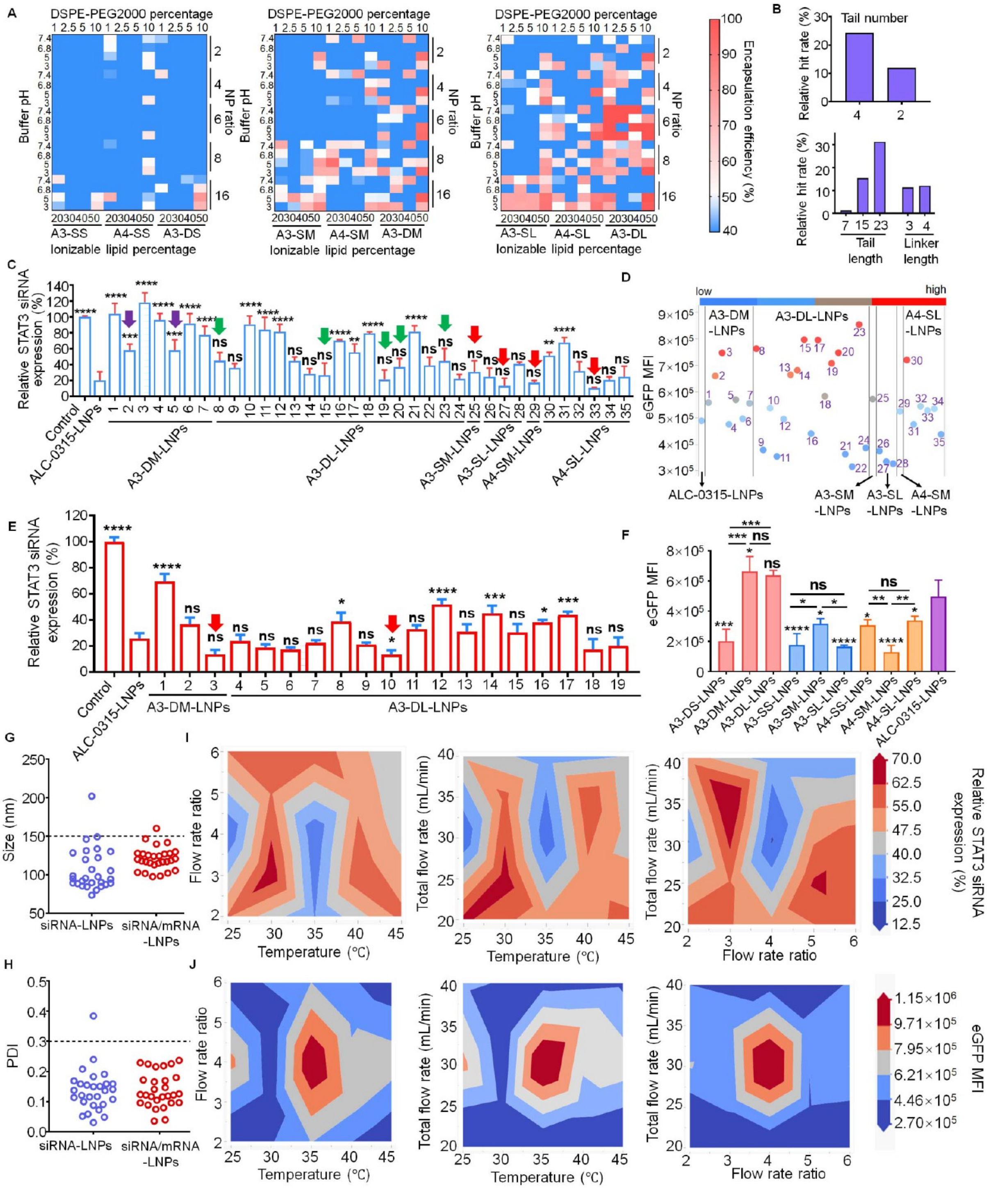

Figure 2. Multistep screening and optimization of LNP formulations via microfluidic preparation. (**A**) A heatmap illustrates siRNA and mRNA encapsulation efficiency across 720 lipid nanoparticle (LNP) formulations, quantified using RiboGreen assays. The top 35 formulations demonstrating >80% encapsulation efficiency were selected for further evaluation. (**B**) Hit rates were analyzed as a function of ionizable lipid structural features, including tail number, tail length, and linker length. Formulations with encapsulation efficiencies >60% were classified as hits for structural trend analysis. (**C**) In vitro siRNA transfection performance of the 35 candidate formulations was evaluated in DC2.4 cells using siSTAT3-loaded LNPs (*n* = 3), with STAT3 knockdown quantified 24 h post-treatment. Based on predefined physicochemical thresholds (particle size < 150 nm and PDI < 0.3, see Figure S11) and functional performance, formulations within the optimal performance window were identified (indicated by arrows) for further consideration. Meanwhile, (**D**) dot plot analysis of GFP mRNA expression levels was performed for A3-DM, A3-DL, A3-SM, A3-SL, A4-SM, and A4-SL-LNPs, with ALC-0315-LNPs serving as the positive control. (**E**−**F**) Based on the combined assessment of siRNA silencing efficiency and mRNA expression, lead formulations from the A3-DM and A3-DL series were further evaluated for (**E**) siRNA-mediated gene silencing and (**F**) mRNA-driven protein expression (*n* = 3). (**G**−**H**) Microfluidic process parameters were systematically optimized by evaluating particle size and polydispersity index (PDI) of LNPs encapsulating either siRNA or mRNA. (**I**−**J**) Contour plots showed the influence of microfluidic parameters on the transfection efficiency of A3-DM-LNPs delivering (**I**) siSTAT3 and (**J**) GFP-encoding mRNA. Data in

Figure 2. continued

panels C, E and F are presented as mean ± SD. Statistical analysis was performed using one-way ANOVA with Dunnett's multiple comparisons test against the ALC-0315 control. Significance levels: $^{*}P < 0.05$; $^{**}P < 0.01$; $^{***}P < 0.001$; $^{****}P < 0.0001$; ns, not significant.

chains could facilitate the formation of finely tuned non-lamellar phase LNPs capable of potent coencapsulation of mRNA and siRNA.[36,37] Imidazole, imidazolium, and dihydroimidazole moieties—aromatic heterocycles with protonatable amphiphilic amine functionality—offer a diverse chemical framework conducive to efficient RNA delivery.[38−41] Additionally, the rigid and chemically reactive nature of piperazine, a cycloalkane-based polar linker, provides structural stability and optimal spatial geometry for multialkyl-chain lipid components, enabling effective interactions with RNA therapeutics.[42,43] In contrast to linear ester-linked ionizable lipids including MC3, ALC-0315 and SM-102 in FDA-approved formulations, our study introduces a series of rationally designed bipolar ionizable lipids. These molecules incorporate a piperazine linker fused to backbone-alkylated dihydroimidazole units, varying in alkyl chain length and symmetry. Using this strategy, we synthesized a series of ionizable lipids comprising three distinct hydrophilic headgroup architectures (A3-D, A3-S, and A4-S) and three alkyl tail variants (S, M, and L) via a multicomponent condensation reaction involving piperazine amines, ethyl isocyanoacetate, and alkyl ketones (Figure 1). The hydrophobic tail variants S, M, and L correspond to carbon chain lengths of 3, 7, and 11 carbons, respectively. In terms of headgroup architecture, A3-D lipids adopt a symmetric bipolar configuration, in which identical piperazine-linked substituents are present on both sides of the core scaffold, whereas A3-S and A4-S lipids feature a single-tailed configuration. In addition, the piperazine linker carbon chain length differs among the headgroup architectures, being 3 carbons for A3-D and A3-S lipids and 4 carbons for A4-S lipids. The ionizable lipid materials were then purified by flash column chromatography and characterized by ^{1}H NMR (see Figures S1−S9 for detailed characterization).

Systematic Screening and Optimization of LNP Formulation for Enhanced RNA Delivery

To identify an optimal LNP formulation for efficient RNA delivery, we systematically investigated the composition of LNP formulations by varying the weight ratio of bipolar ionizable lipids, cholesterol, DSPE-PEG2000, and helper lipids (DSPC, DOPC, DMPC, or DPPC). The flowchart (Figure S10) illustrates the basic process of our formulation screening, which consists of three rounds of optimization. In the first round, we created an initial library of 720 LNP formulations using an orthogonal experimental design, varying parameters such as the ionizable lipid percentage, cholesterol, N/P ratio, and pH as follows: (1) weight percentage of bipolar ionizable lipids (20−50%); (2) weight percentage of DSPE-PEG2000 (1−10%); (3) weight percentage of cholesterol (10−40%); (4) the molar ratio of amine groups in the ionizable lipid to phosphate groups in RNA therapeutics (N/P ratio: 2−16); (5) aqueous-phase preparation pH (3.0−7.4) (Table S1). Heatmap analysis demonstrated the total siRNA and mRNA encapsulation efficiency across nine ionizable lipid variants (Figure 2A), and hit rate analysis (defined as RNA encapsulation efficiency >60%) identified key formulation parameters influencing RNA loading (Figure 2B). The symmetric bipolar lipids with four alkyl tails (A3-DS/DM/DL) exhibited significantly higher RNA encapsulation efficacy achieving a notable hit rate of 24.2%, as compared to asymmetric lipids with two alkyl tails (A3-SS/SM/SL or A4-SS/SM/SL). Furthermore, encapsulation efficiency positively correlated with tail length; long-chain variants exhibited a 31.3% hit rate, representing 24.1-fold and 2.0-fold improvements over short- and medium-chain derivatives, respectively. However, the piperazine linker length showed no statistically significant impact on encapsulation efficiency (Figure 2B). Dynamic light scattering (DLS) indicated most of these LNPs had a size distribution smaller than 200 nm with the polymer dispersity index (PDI) values less than 0.3 (Figure S11). Tables S2−S6 displays the particle size and PDI values for all 720 formulations, providing a detailed overview of the distribution and characteristics of the LNPs. Given the crucial role of acid dissociation constant (pK_a) in determining surface charge, ionization behavior, and ultimately RNA encapsulation, cellular uptake, and biodistribution,[44−46] we measured the apparent pK_a values using the TNS assay (Figure S12). Prior studies have shown that LNPs with low apparent pK_a values (2.0−6.0) favor spleen-specific RNA delivery.[47] In our system, incorporation of bulky polar head groups and four alkyl tails resulted in pK_a values ranging from 5.46 to 7.99, higher than those observed for asymmetric two-tailed lipids, suggesting enhanced RNA delivery potential for these structurally optimized LNPs.[45]

In the first round of screening, we prioritized RNA encapsulation efficiency (>80%), particle size (<200 nm), and PDI (<0.3) to ensure optimal formulation characteristics. High RNA encapsulation efficiency is crucial for effective RNA delivery, while a particle size below 200 nm enhances cellular uptake and in vivo circulation. A low PDI ensures uniform nanoparticle size for consistent delivery. These criteria helped us select the most promising formulations for further evaluation of siRNA silencing efficiency and mRNA expression. From the initial formulation library, the top 35 candidates (Table S7 and Figure S11), meeting these criteria, were selected for transfection performance screening in DC2.4 cells in vitro. As a benchmark, we included the clinically validated ALC-0315-LNP formulation. Primary screening identified four lead formulations (#25, 27, 29, 33), containing A3-SM, A3-SL, A4-SM, and A4-SL lipids, which achieved over 70% STAT3 gene silencing efficiency and robust mRNA-derived protein expression, similar to ALC-0315-LNPs (Figure 2C−D). A3-DM formulations (#2 and #5) showed balanced STAT3 silencing and GFP expression, and A3-DL formulations (#8, 15, 19, 20, and 23) demonstrated favorable properties like smaller particle size and efficient gene silencing (Figure 2C−D). Among them, #2 and #5 for A3-DM-LNPs showed better mRNA expression, while #19 and #23 for A3-DL-LNPs demonstrated a balance between siRNA silencing and mRNA expression. Based on these results, formulations #2 and #5 (A3-DM-LNPs) and #19 and #23 (A3-DL-LNPs) were selected for further optimization in the second round due to their superior delivery efficiency. A3-SM-LNPs, A3-SL-LNPs, A4-SM-LNPs, and A4-SL-LNPs only had one preferred formulation identified in the first round, so no further optimization was done in the second round.

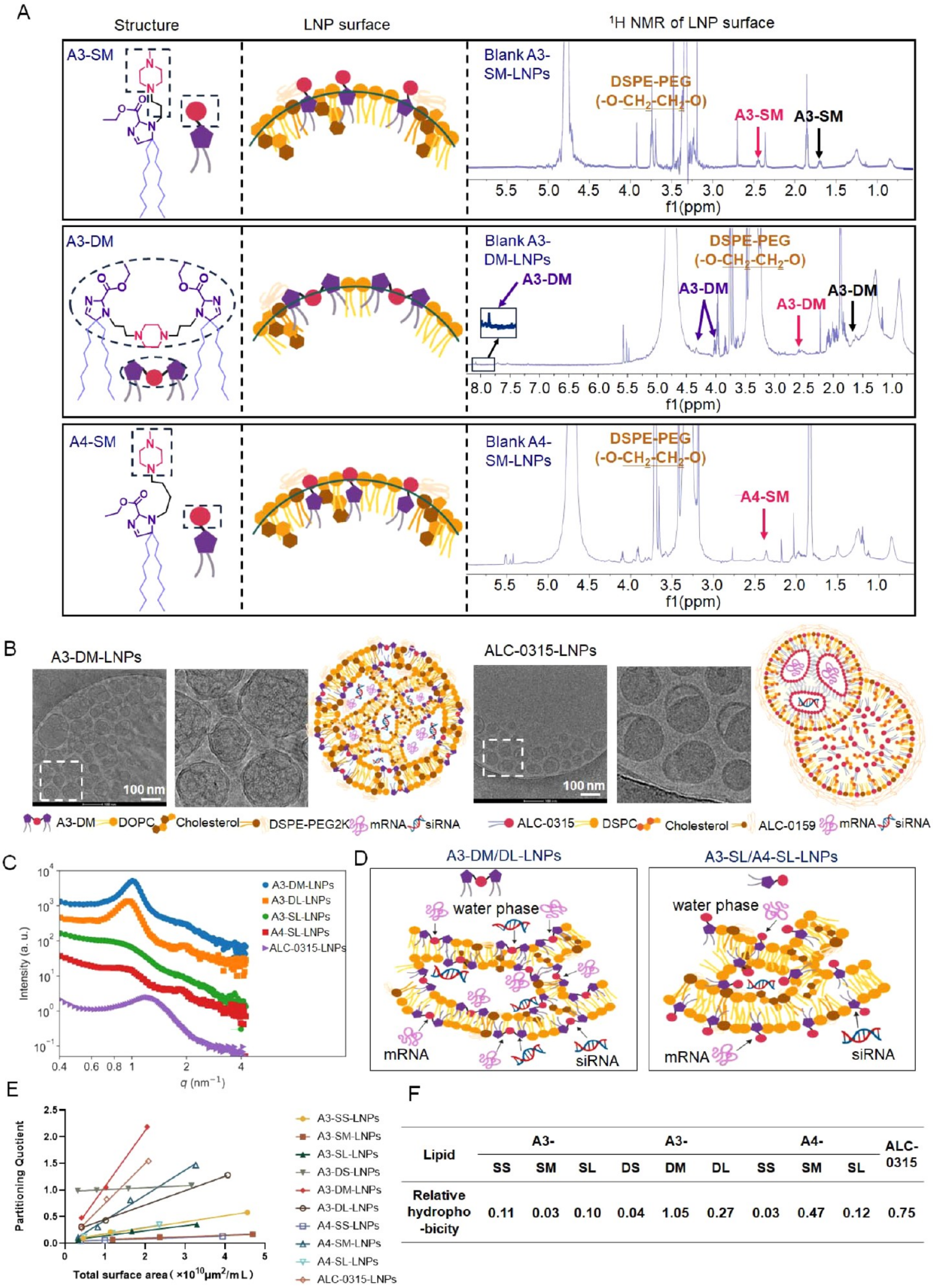

Lipid	A3-			A3-			A4-			ALC-0315
	SS	SM	SL	DS	DM	DL	SS	SM	SL	
Relative hydrophobicity	0.11	0.03	0.10	0.04	1.05	0.27	0.03	0.47	0.12	0.75

Figure 3. The effect of imidazole-based ionizable lipid type on LNP structure. (**A**) From left to right, a schematic illustration showed the hypothetical architecture of imidazole-based ionizable lipids on the LNP surface, highlighting the spatial organization of lipid components, including helper lipids, cholesterol, and PEGylated lipids. Structural and surface characteristics of intact blank A3-SM, A3-DM and A4-SM-LNPs were subsequently analyzed using ^{1}H NMR spectroscopy, providing insights into lipid distribution and surface composition. The detected surface protons of A3-SM, A3-DM, and A4-SM were annotated on their respective molecular structures in purple, pink, and black. (**B**) Cryo-TEM images of A3-DM-LNPs and ALC-0315-LNPs coencapsulating siRNA and mRNA. Micrographs represent a selected field from a single experiment. (**C**) SAXS profiles of A3-DM-, A3-DL-, A3-SL-, A4-SL-, and ALC-0315-LNPs coloaded with siRNA and mRNA, revealing formulation-dependent differences in internal organization. Imidazole-based A3-DM- and A3-DL-LNPs exhibit pronounced broad correlation peaks in the intermediate q range, indicative of quasi-periodic, multicompartment internal structures, whereas ALC-0315-LNPs display a smooth scattering decay consistent with a more homogeneous, amorphous core. (**D**) Schematic representation of the proposed interactions between A3-DM/DL-LNPs and A3-SL/A4-SL-LNPs with RNA therapeutics, where the multicompartmental architecture potentially overcomes traditional lamellar and bleb structure

Figure 3. continued

limitations for RNA encapsulation. (**E**−**F**) Relative surface hydrophobicity of LNPs assessed by Rose Bengal adsorption displayed differences in surface chemistry among formulations. All illustrations in the panels were created using BioRender.com.

In the second round of optimization, A3-DM-LNPs were refined by fixing the ionizable lipid content at 40%, retaining DOPC as the helper lipid, and systematically varying the cholesterol-to-helper lipid ratio (1:2, 1:1, and 2:1). For A3-DL-LNPs, the cholesterol content was fixed at 40% and the N/P ratio at 6, while other formulation parameters were adjusted within the ranges defined by formulations #19 and #23, enabling further exploration of the local formulation space (Table S8). As a result of this refinement, the optimized A3-DM-LNPs (#3, red arrow) and A3-DL-LNPs (#10, red arrow) exhibited 4.0-fold and 3.1-fold higher mRNA expression levels, respectively, compared to the ALC-0315 control, while maintaining particle sizes below 150 nm (Figures 2E−F and S13). The exact compositions of the optimized A3-DM-LNP and A3-DL-LNP formulations used for the in vivo studies are defined based on molar ratios. Specifically, the molar ratio of ionizable lipid/cholesterol/DSPE-PEG2000/DOPC was 28.3/57.0/1.1/13.6 for A3-DM-LNPs and 16.8/61.8/0.5/20.9 for A3-DL-LNPs. The corresponding weight percentage compositions are provided in Table S8 for reference. Together, these results demonstrate that second-round formulation refinement substantially enhances mRNA delivery performance in dendritic cells while preserving favorable physicochemical properties.

Microfluidic Protocol for LNP Formulations

To optimize the large-scale production of LNP formulations, the key microfluidic parameters including total flow rate (TFR), flow rate ratio (FRR), and temperature were screened using a single-factor experimental design in the third-round screening. Experiments were conducted with the Small Dragon Mixer (SDM) microfluidic chips integrated into the INano L/L+ platform (Micro&Nano Biologics Co., Ltd.) (Figure S14). Based on initial screening for particle size and polydispersity index (PDI), the factor ranges were refined as detailed in Table S9. A second round of screening was then carried out using in vitro transfection assays with A3-DM-LNPs as the model formulation coloaded with mRNA and siRNA. A three-factor, five-level design was applied, testing: (1) TFR values from 20 to 40 mL/min; (2) FRR values from 2:1 to 6:1; and (3) formulation temperatures ranging from 25 to 45 °C. Notably, preparation parameters had a more pronounced effect on the size and PDI of siRNA-only LNPs compared to those coloaded with mRNA and siRNA under identical conditions (Figure 2G−H). Under optimized conditions, A3-DM-LNPs (siRNA/mRNA-LNPs) achieved a STAT3 gene silencing efficiency of 80%, while eGFP mRNA expression reached an average fluorescence intensity of 1.44×10^6 in DC2.4 cells (Figure 2I−J). These results establish a robust and scalable microfluidic protocol with TFR of 30 mL/min, FRR of 4:1, and temperature of 35 °C as optimal conditions for consistent preparation of high-performance LNPs for RNA codelivery.

Structural Multiplicity of Disordered Multicompartment Phase Separation in Imidazole-Based LNPs

To elucidate the effect of molecular organization and interfacial dynamics of LNPs assembled from different ionizable lipid moieties on RNA encapsulation and transfection, we performed solution-state NMR spectroscopy to characterize their outer layer structures and lipid distribution profiles.[48,49] Although the imidazole-based ionizable lipids employed in our formulations remain in a liquid state at room temperature due to their low melting points, they demonstrated distinct dynamic profiles at the membrane surface. In all LNP formulations, the ^{1}H NMR signal of the PEG moiety (∼3.7 ppm) displayed a consistent downfield shift, suggesting strong interactions between the PEG chains and other excipients at the LNP's hydrophilic interface upon RNA encapsulation (Figure S15−S23). In blank A3-DM/DL-LNPs, the H3 peak, corresponding to the carbon−nitrogen double bond in dihydroimidazole, was clearly observed, whereas it was masked following RNA loading, indicating successful encapsulation within the LNP core (Figures 3A, S15 and S16). Notably, the broad proton peaks of the piperazine moiety (H1, H2 ∼ 2.5 ppm) were detected in A3-DM but not A3-DL formulations, suggesting different spatial orientations of the piperazine linker. We speculate that the increased alkyl chain length in A3-DL enhances lipid flexibility and promotes embedding of the piperazine group toward the hydrophobic interface, facilitating the formation of an "M-shaped" headgroup that contributes to improved RNA delivery efficiency (Figures 2, S15 and S16). In contrast, for blank A3-DS-LNPs, proton signals from H1, H2, and H5 were present on the surface and disappeared upon RNA complexation, further supporting the hypothesis that RNA encapsulation triggers surface conformational rearrangements in A3-DS/DM/DL-LNPs (Figure S17). NMR spectra of LNPs formulated with two-tailed lipids (A3-SS/SM/SL and A4-SS/SM/SL) revealed that piperazine groups were exposed to the aqueous interface, while the dihydroimidazole or secondary/tertiary amine segments localized to the hydrophobic membrane interior with reduced mobility (Figures S18−S23).

To further investigate LNP morphology, we performed cryogenic transmission electron microscopy (cryo-TEM) on LNPs formulated with nine designed bipolar ionizable lipids, alongside ALC-0315-LNPs as a control. Cryo-TEM micrographs revealed that LNPs with large polar headgroup lipids exhibited a distinct multicompartmentalized core and a thin peripheral lamellar structure, while ALC-0315-LNPs formed a bleb uniform lamellar on the surface with an amorphous core (Figures 3B and S24A). These images provide direct visual confirmation of formulation-dependent mesoscopic structure differences of LNPs particles. Importantly, long-term stability studies showed that both A3-DM-LNPs and A3-DL-LNPs maintained consistent particle size and PDI over 30 days of storage at 4 °C, with no evidence of aggregation or structural transition, supporting the sustained preservation of their multicompartment architecture (Figure S24B−D). However, given the inherently limited sampling of Cryo-TEM, quantitative structural observations are primarily supported by ensemble-averaged scattering measurements.

Accordingly, the mesoscopic internal organization of the LNPs was quantitatively characterized using SAXS, which probes structural correlations across a statistically large population of particles in solution. The scattering profiles of imidazole-based LNPs were analyzed using the Teubner−Strey (T-S) model, a well-established approach for characterizing

https://doi.org/10.1021/jacs.5c23209
J. Am. Chem. Soc. XXXX, XXX, XXX−XXX

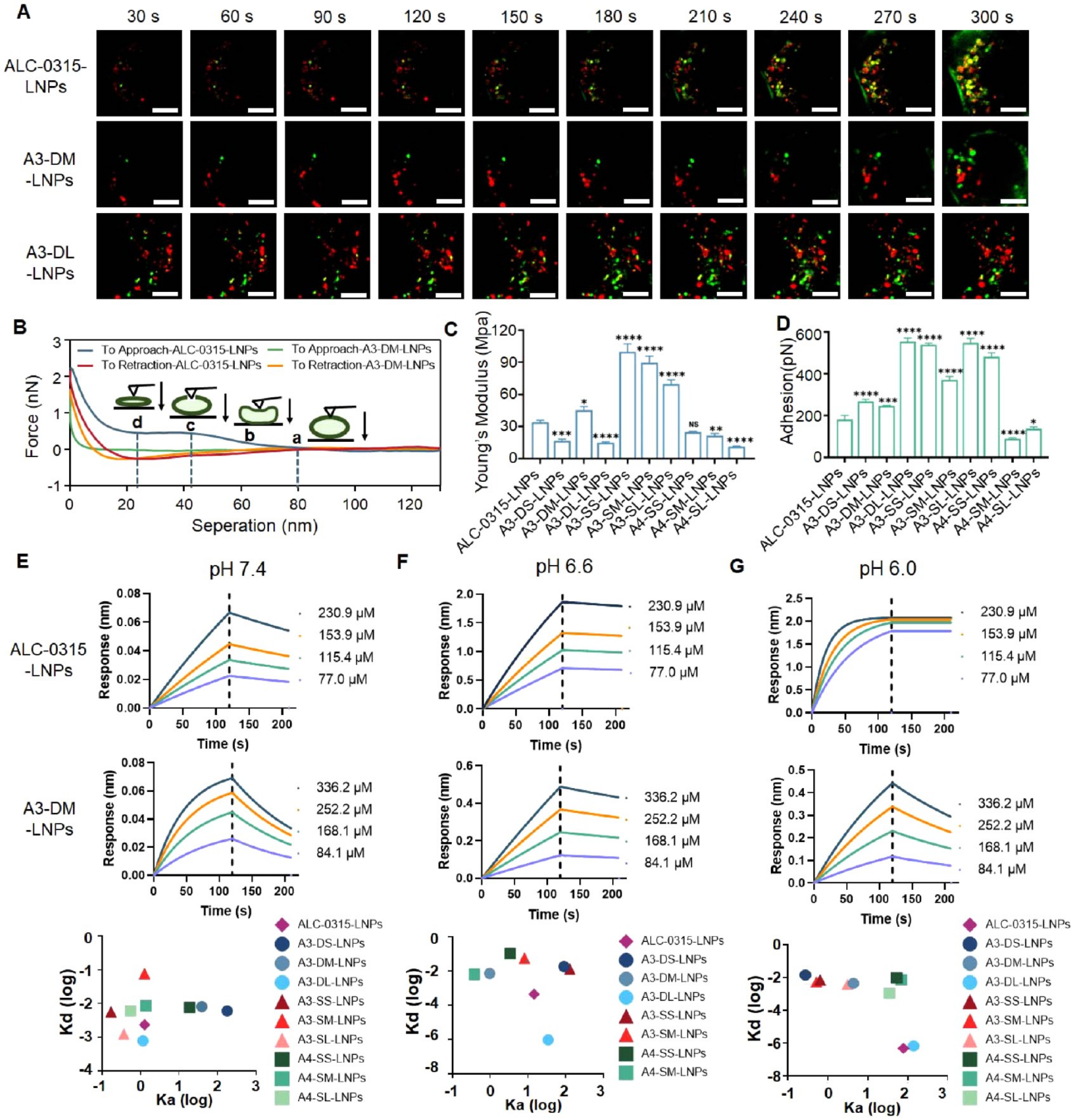

Figure 4. Imidazole-based LNPs enable efficient RNA delivery by enhancing membrane affinity and cellular uptake. (**A**) Representative images showing cellular uptake of FITC-labeled ALC-0315-LNPs, A3-DM-LNPs, and A3-DL-LNPs in DC 2.4 cells, acquiring images every 30 s using a Polar-SIM High-fidelity Polarized Super-Resolution Microscopy. Lysosomes were stained with LysoTracker Red. Scale bar is 5 μm. (**B**) Typical force−distance curves for ALC-0315-LNPs and A3-DM-LNPs, obtained using atomic force microscopy (AFM) via an approach-dwell-retract cycle with the AFM tip engaging vertically with the LNPs. Alphabetically labeled schematic diagrams along the curves illustrate distinct phases of AFM-LNP interaction for ALC-0315-LNPs: (a) initial contact between the tip and the LNP surface; (b) progressive compression of the LNP by the tip; (c) irreversible rupture of a surface-associated water bleb; and (d) penetration into the amorphous lipid core. These phases highlight key mechanical responses and transition points during the indentation process. (**C**) Quantitative comparison of Young's modulus for different LNP formulations, derived from the contact region of the force−distance curves ($n = 3$). (**D**) Statistical analysis of the adhesion force observed during tip retraction for the various LNP formulations ($n = 3$). (**E−G**) Influence of LNP concentration, ionizable lipid composition, and pH on LNP-DC2.4 membrane interactions. Binding kinetics of various LNP formulations to DC2.4 cell membranes were evaluated under different pH conditions (pH 7.4, 6.6, 6.0, and 5.6) in HEPES buffer, with varying LNP concentrations. Binding curves were generated to monitor the association and dissociation phases of LNP-membrane interaction. The effects of ionizable lipid type and environmental pH on membrane affinity were assessed. For each LNP formulation, the log-transformed association constant (K_a) and dissociation constant (K_d) were determined, reflecting the binding strength and stability under different physicochemical conditions. Data are presented as mean ± SD. Statistical analysis was performed using one-way ANOVA. Significance levels: ns, not significant; $*P < 0.05$; $**P < 0.01$; $***P < 0.001$; $****P < 0.0001$.

microemulsion-like phase separations.[50] In contrast, the scattering profile of ALC-0315-LNPs was interpreted using Bragg-type peak analysis, in which the characteristic real-space distance associated with the dominant q maximum was calculated as 4.5−4.8 nm. This characteristic distance was in good agreement with previously reported scattering features of mRNA encapsulated LNPs. For A3-DM and A3-DL-LNPs, the SAXS profiles showed more pronounced correlation peaks in the intermediate q-range, indicating an enhanced quasi-periodic internal nanostructure relative to ALC-0315-LNPs. Ensemble-level validation of internal compartmentalization potentially can effectively substitute the manual compartment counting from electron micrographs. The corresponding domain spacings (d) were 3.42 nm (A3-DM-LNPs) and 3.17 nm (A3-DL-LNPs), both were smaller than that of ALC-0315-LNPs (4.5 ∼ 4.8 nm), indicating a more densely packed internal architecture. This observation was consistent with that of cryo-TEM (Figure 3C−D). Notably, the I-q curves of A3-DM/DL-LNPs exhibited two diffraction peaks with a position ratio of approximately 1:2, a distinct peak at $q \sim 1\ \mathrm{nm}^{-1}$ and a weaker peak at $q \sim 2\ \mathrm{nm}^{-1}$, indicating higher-order internal correlations consistent with quasi-periodic domain spacing in a sponge-like internal organization. The absence of well-resolved higher-order Bragg peaks further confirmed that the imidazole-based LNPs structures do not exhibit long-range liquid-crystalline order.

Fitting the scattering profile with the T-S model obtained correlation lengths (ξ) of 1.74 nm for A3-DM-LNPs and 4.22 nm for A3-DL-LNPs, suggesting stronger lipid-RNA interaction and enhanced encapsulation efficiency in A3-DL-LNPs, results from the longer hydrophobic tail of the ionizable lipid. By comparison, the A3-SL-LNPs and A4-SL-LNPs displayed a broader and less defined scattering peak at q range of 0.9 ∼ 1.0 nm^{-1}, which is distinct from the sharper peaks observed in A3-DM-LNPs and A3-DL-LNPs. This suggests that while A3-SL-LNPs and A4-SL-LNPs retain some degree of short-range nanoscale ordering, their internal structure is more disordered and lacks long-range periodicity, aligning with a loosely packed and sponge-like morphology. The fitted correlation lengths further support this interpretation, with a ξ value of 1.61 and 3.01 nm for A3-SL-LNPs and A4-SL-LNPs respectively (Figures 3C and S25). Additionally, surface hydrophobicity, evaluated using the Rose Bengal partitioning method, revealed that A3-DM-LNPs were the most hydrophobic, followed by ALC-0315-LNPs, A4-SM-LNPs, A3-DL-LNPs, and a cluster of similarly ranked formulations including A4-SL-LNPs, A3-SS-LNPs, and A3-SL-LNPs. Lower hydrophobicity was observed for A3-DS-LNPs, with the least hydrophobic being A3-SM-LNPs and A4-SS-LNPs (Figure 3E−F). These results suggest that increased surface hydrophobicity likely contribute to the enhanced transfection efficiency observed in A3-DM/DL-LNPs. Collectively, these findings emphasize that the interfacial dynamics and internal architecture of chemically diverse ionizable lipids critically govern phase behavior, lipid-RNA interactions, and, ultimately, RNA encapsulation and delivery efficacy.

Imidazole-Based LNPs Facilitate Cytosolic Delivery of RNA Cargos

To investigate whether the superior RNA delivery efficiency of imidazole-based LNPs is attributable to their surface conformation, multicompartment structure, or nanomechanical properties, we first examined their intracellular trafficking behavior, with a particular focus on endosomal trapping and lysosomal escape, using live-cell fluorescence imaging. Super-resolution imaging of lysosomal structures was performed using Polar-structured illumination microscopy, a next-generation wide-field imaging technique offering ultrahigh speed, resolution, and long-term imaging capabilities.[51] As shown in Figure 4A, ALC-0315-LNPs exhibited strong and persistent colocalization with LysoTracker Red, as evidenced by prominent yellow fluorescence, indicating pronounced endosomal/lysosomal sequestration, a process known to limit cytosolic cargo release and reduce therapeutic efficacy.[52,53] In contrast, A3-DL-LNPs displayed progressively enhanced fluorescein isothiocyanate (FITC) signals in the cytoplasm accompanied by reduced lysosomal overlap, suggesting more efficient endolysosomal escape following cellular uptake. Similarly, A3-DM-LNPs showed minimal lysosomal colocalization together with strong cytoplasmic fluorescence, indicative of limited endosomal trapping and effective cytosolic redistribution. Quantitative analysis further supported these observations: the Pearson's correlation coefficients (R values) between lysosomes and ALC-0315-LNPs, A3-DM-LNPs, and A3-DL-LNPs were 0.72, 0.17, and 0.36, respectively. In comparison, A3-SL-LNPs and A4-SL-LNPs exhibited weak cytoplasmic fluorescence, reflecting poor cellular uptake and inefficient intracellular delivery (Figure S26). Collectively, these results indicate that imidazole-based A3-DM and A3-DL-LNPs experience reduced endosomal trapping and achieve more efficient cytosolic delivery, likely facilitated by the "M-shaped" conformation formed by their imidazole- and piperazine-containing polar headgroups.

To further examine whether particle rigidity contributes to uptake efficiency, we assessed the nanomechanical properties of the LNPs using liquid-phase atomic force microscopy (AFM). All formulations displayed uniform size distribution consistent with cryo-TEM observations (Figure S27). Force−distance spectroscopy revealed differences in stiffness, elasticity, and adhesion across LNP types (Figures 4B and S28). The approach curve of ALC-0315-LNPs displayed a sudden drop in force (phase c), consistent with rupture of the blebbed surface structure and efflux of internal fluid. Compression beyond one-third of the particle height led to a steep rise in force, indicating probe contact with the dense lipid core (Figures 4B and S28). In contrast, all imidazole-based LNPs showed force−distance curves lacking rupture signatures, indicating resistance to probe penetration and suggesting a gel-like internal state with improved mechanical stability compared to ALC-0315-LNPs.[54] For imidazole-based LNPs with two-tailed lipid architectures (A3-SS/SM/SL and A4-SS/SM/SL), Young's modulus decreased with increasing alkyl chain length. Among these, A3-SS-, A3-SM-, and A3-SL-LNPs exhibited significantly higher rigidity (69.8−99.8 MPa), roughly 2−3 times that of ALC-0315-LNPs (34.1 MPa). In contrast, A4-SM/SL-LNPs were mechanically softer than ALC-0315. Interestingly, A3-DM-LNPs exhibited a 32% increase in Young's modulus, while A3-DL-LNPs showed a 50% reduction, relative to ALC-0315-LNPs (Figure 4C). Moreover, bulky polar head-containing LNPs generally exhibited stronger adhesion than ALC-0315-LNPs, except for A4-SM/SL-LNPs, yet no strong correlation with uptake efficiency was observed (Figure 4D). Taken together, these findings indicate that neither stiffness nor adhesion is the dominant factor driving enhanced cytosolic delivery in imidazole-based LNPs. Instead, the structural features, such as lipid architecture at the particle surface and internal topology, likely play a more critical role in modulating dynamic interactions with cellular membranes and determining intracellular trafficking outcomes.

"M-Shape" Lipid Configuration Enhances LNP-Membrane Interfacial Interaction

To assess whether the superior RNA delivery efficiency of imidazole-based LNPs is related to their surface architecture, multicompartment morphology, and membrane interaction kinetics, we employed biolayer interferometry (BLI) to quantify the association and dissociation behavior of LNPs with DC2.4 cell membranes under various pH conditions (Figure S29). The DC2.4 cell membrane was used to simulate the biological interface of membrane-bound vesicles, such as caveosomes, endosomes, and macropinosomes, that mediate LNP uptake via endocytic pathways.[55] LNPs prepared at different pH values were evaluated to determine how pH-dependent structural or phase changes may influence membrane interaction[56] (Figure S30). Among the tested formulations, four-tail imidazole-based LNPs (A3-DS/DM/DL-LNPs) exhibited the strongest membrane-binding affinity at physiological pH of 7.4, as reflected by the lowest equilibrium dissociation constants (K_D), significantly outperforming ALC-0315-LNPs (Figure 4E−F and Table S10). This suggests that multicompartment LNPs more effectively interact with the plasma membrane, contributing to enhanced uptake. In contrast, LNPs formulated with two-tail lipids bearing bulky polar headgroups showed generally weaker membrane affinity, except for A4-SS-LNPs. The BLI association phase also revealed distinct kinetic profiles. A3-DM-LNPs exhibited rapid association kinetics, whereas ALC-0315-LNPs showed a slower membrane-binding rate (Figure 4E and Table S10). Remarkably, the presence of "M-shape" lipid configuration in A3-DM-LNPs conferred a dramatically higher binding affinity (K_D = 2.09 × 10^{-4} M, K_a = 38.9 $M^{-1}s^{-1}$), representing ~9-fold and 30-fold higher affinity compared to ALC-0315-LNPs (K_D = 1.85 × 10^{-3} M, K_a = 1.27 $M^{-1}s^{-1}$), respectively, demonstrating a strong relationship between surface conformation and membrane-binding kinetics.

We next examined how pH influences membrane interaction. At pH 6.6, A3-DM-LNPs exhibited dramatically reduced affinity (K_D = 7.55 × 10^{-3} M, K_d = 7.25 × 10^{-3}/s), approximately 250-fold and 16.5-fold higher than ALC-0315-LNPs (K_D = 3.02 × 10^{-5} M, K_d = 4.39 × 10^{-4}/s) at pH 6.6, indicating a pronounced pH sensitivity and diminished membrane association (Figure 4F and Table S10). At pH 6.0, A3-DM-LNPs displayed an even greater reduction in affinity, with K_D and K_d values several orders of magnitude higher than those of ALC-0315-LNPs (Figure 4G). In contrast, ALC-0315-LNPs retained measurable binding affinity at acidic pH, with saturation occurring at relatively high concentrations of 153.9 μM and 230.9 μM at pH 6.0. Notably, ALC-0315-LNPs showed increasing affinity under acidic conditions, with K_D decreasing to 3.61 × 10^{-9} M and K_d to 9.77 × 10^{-7}/s at pH 5.6 (Table S10 and Figure S31), consistent with a pH-triggered transition from a lamellar to inverted hexagonal phase that facilitates lysosomal escape.[33] While this transition may improve membrane fusion and endosomal escape for ALC-0315-LNPs, prior studies have shown that a substantial portion of RNA cargo remains sequestered in RNA-lipid complexes.[57,58] In contrast, A3-DM-LNPs demonstrated limited affinity for membranes under acidic conditions, which may reduce endosome-lysosome interaction and help circumvent lysosomal degradation. Consistent with live-cell fluorescence imaging results (Figure 4A), A3-DM-LNPs exhibited enhanced cytoplasmic signal with minimal lysosomal colocalization, suggesting entry via caveolae-mediated endocytosis, thereby redirecting intracellular trafficking away from lysosomal pathways and enhancing cytosolic delivery.

Interestingly, A3-DL-LNPs showed similar membrane-binding affinity to ALC-0315-LNPs at pH 6.0 (K_D = 4.91 × 10^{-9} M, K_d = 6.79 × 10^{-7}/s), while at pH 6.6, both K_D (2.75 × 10^{-8} M) and K_d (9.45 × 10^{-7}/s) were approximately 3 orders of magnitude higher than those of ALC-0315-LNPs. These kinetic properties correlate well with imaging results, where A3-DL-LNPs displayed enhanced cellular uptake and limited lysosomal localization compared to ALC-0315-LNPs. The cytosolic delivery capabilities of A3-DM and A3-DL-LNPs were further validated using both pharmacological inhibition and genetic perturbation of cellular uptake pathways, and assessed via confocal microscopy (Figures S32−S34). In addition to inhibitor-based studies, siRNA-mediated knockdown of caveolin-1 in DC2.4 cells led to a pronounced reduction in the uptake of FITC-labeled A3-DM and A3-DL-LNPs, whereas the uptake of ALC-0315-LNPs was minimally affected (Figure S34B). Together, these results indicate that the enhanced membrane affinity of A3-DM/DL-LNPs contribute to reduced lysosomal sequestration, efficient cytosolic delivery, and effective RNA payload release.

Diffusivity and Penetration of LNP Formulations

To mechanistically link the unique physicochemical properties of imidazole-based multicompartment LNPs with their enhanced tissue penetration and immune-organ targeting observed in vivo, we next employed confocal laser scanning microscopy (CLSM)-based multiparticle tracking within collagen hydrogel matrices, which served as a mimic of extracellular matrix (ECM)[59] and their ability to traverse endothelial barriers. Representative particle trajectories revealed that A3-DS/DM-LNPs and ALC-0315-LNPs exhibited limited mobility, whereas A3-DL-LNPs demonstrated markedly enhanced motility and the greatest diffusion capacity among all tested formulations (Figure S35A). This was supported by significantly higher ensemble-averaged geometric mean-squared displacement (MSD) values for A3-DL-LNPs compared to the other groups (Figure S35B), as well as the broadest distribution of effective diffusivities (Deff), indicating superior diffusive behavior (Figure S35C).

Because endothelial tight junctions constitute a major physical barrier to nanoparticle extravasation and access to immune organs, we employed trans-endothelial electrical resistance (TEER) measurements to evaluate whether imidazole-based LNPs could transiently modulate endothelial barrier integrity. To assess the ability of different LNP formulations to alter endothelial barrier function, TEER was measured from both the apical and basal sides of human umbilical vein endothelial cell (HUVEC) monolayers. Apical exposure to A3-DM/DL-LNPs induced a significant, time-dependent decrease in TEER, comparable to the effect of chitosan, a known tight junction disruptor that promotes cytoskeletal reorganization of junctional proteins[60,61] (Figure S35D). In contrast, ALC-0315-LNPs did not significantly alter TEER or enhance the translocation of D-luciferin potassium salt over 12 h (Figure S35E). These findings suggest that A3-DM/DL-LNPs facilitate enhanced paracellular cargo transport

https://doi.org/10.1021/jacs.5c23209
J. Am. Chem. Soc. XXXX, XXX, XXX−XXX

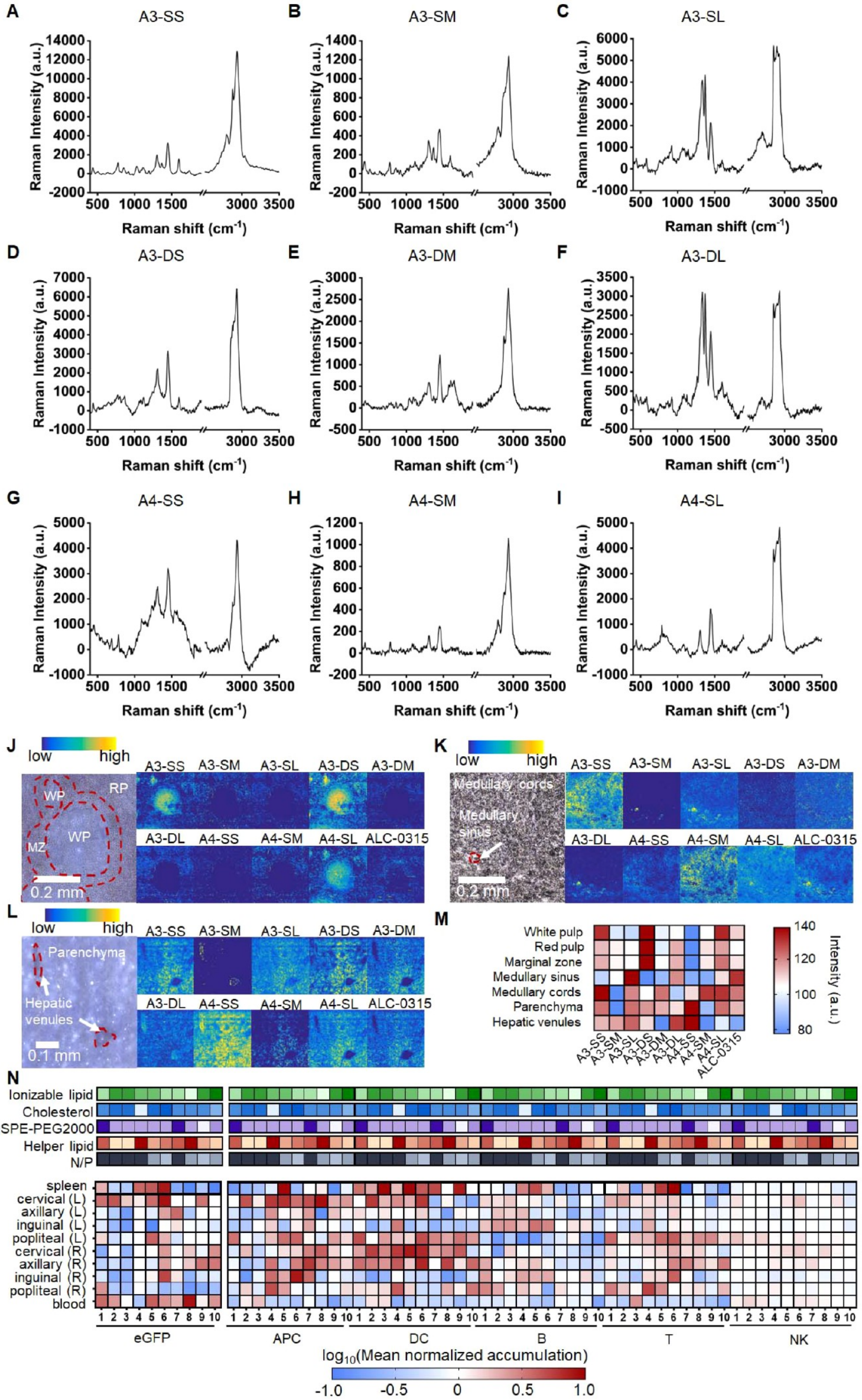

Figure 5. Fingerprint-region Raman spectra and label-free lipid imaging in tissues. Raman spectra of various ionizable lipids in the fingerprint region: (**A**) A3-SS, (**B**) A3-SM, (**C**) A3-SL, (**D**) A3-DS, (**E**) A3-DM, (**F**) A3-DL, (**G**) A4-SS, (**H**) A4-SM, and (**I**) A4-SL, highlighting characteristic vibrational modes for structural differentiation. Label-free Raman spectral imaging of identified lipids including A3-SS/SM/SL, A3-DS/DM/DL, A4-SS/SM/SL and ALC-0315 in the same mouse (**J**) spleen, (**K**) lymph node, and (**L**) liver following intravenous injection of ten pooled LNP formulations for 6 h, demonstrating spatial lipid distribution in each tissue. (**M**) Quantitative analysis of lipid abundance across the different organs. Afterward, (**N**) eGFP mRNA-loaded LNPs, formulated with nine imidazole-based ionizable lipids, were intravenously administered to C57BL/6J mice, with ALC-0315-LNPs serving as the positive control. At 24 h postinjection, mRNA expression and the activation

Figure 5. continued

status of APCs, DCs, B cells, T cells, and NK cells were analyzed by flow cytometry in the spleen, blood, and draining lymph nodes, including cervical, axillary, inguinal, and popliteal nodes from both the left (L) and right (R) sides (n = 3). Numerical labels at the bottom of heatmap correspond to the following LNP formulations: 1: A3-SS-LNPs, 2: A3-SM-LNPs, 3: A3-SL-LNPs, 4: A3-DS-LNPs, 5: A3-DM-LNPs, 6: A3-DL-LNPs, 7: A4-SS-LNPs, 8: A4-SM-LNPs, 9: A4-SL-LNPs, 10: ALC-0315-LNPs.

through transient modulation of tight junction integrity. To further investigate the effects on tight junction architecture, ZO-1 immunofluorescence staining was performed following 2 h LNP treatment. CLSM imaging showed that imidazole-based LNPs caused reduced intensity and discontinuity of ZO-1 staining, in contrast to the continuous and intact staining pattern observed in PBS-treated controls and the ALC-0315-LNP group (Figure S36). These results demonstrate that imidazole-based LNPs promote localized opening of endothelial tight junctions, enabling effective nanoparticle penetration across the endothelial barrier, thereby offering a promising strategy to enhance RNA therapeutic delivery. Together with the increased extracellular matrix diffusivity, this transient modulation of endothelial barrier integrity provides a coherent mechanistic rationale for the potentially superior in vivo performance of A3-DM/DL-LNPs, including enhanced tissue penetration and improved immune-organ accumulation.

Linking In Vivo Lipid Disposition to Immune-Organ Targeting by Raman Spectral Imaging

While in vitro assays revealed enhanced membrane interaction, diffusivity, and endothelial translocation of A3-DM/DL-LNPs, it remained uncertain whether these advantages translate into altered tissue-level behaviors in vivo.[62,63] To directly visualize and compare the spatial fate of structurally distinct ionizable lipids following systemic administration, we employed Raman spectral imaging, a label-free technique that enables spatial mapping of exogenous lipids based on their intrinsic molecular vibrational signatures. All measurements were performed under identical excitation and acquisition conditions, allowing Raman signal intensity (reported in arbitrary units) to be used for relative, semiquantitative comparison of lipid abundance across tissues and formulations.[64,65]

Characteristic Raman bands corresponding to lipid alkyl chains (850−950, 1000−1200, 1450−1500, and 2850−2950 cm^{-1}), ester functionalities (1000−1200, 1250−1300, and 1720−1750 cm^{-1}), and heterocyclic ring stretching (∼1600 cm^{-1}) enabled unambiguous discrimination of imidazole-based ionizable lipids from ALC-0315 within the same biological system (Figures 5A−I and S37A). Based on reported LNP biodistribution and disassembly kinetics,[66] ten LNP formulations were pooled and intravenously administered to a single Balb/c mouse to allow internally controlled comparison under identical physiological conditions, and tissues were harvested at 6 h postinjection for ex vivo Raman analysis.

Raman imaging revealed pronounced lipid chemistry-dependent differences in tissue distribution at the level of organ microarchitecture. Building on our in vitro findings of enhanced diffusivity and endothelial translocation, we next asked whether these properties translated into immune-organ targeting in vivo; notably, imidazole-based LNPs were preferentially detected in immune-rich regions of the spleen and lymph nodes. In the spleen, A3-SS-, A3-DS-, and A3-DL-LNPs, together with A4-SL-LNPs, displayed strong Raman signals in both the red pulp and marginal zones, regions enriched in DCs, macrophages, B cells, and natural killer (NK) cells.[67] Notably, A3-SS-, A3-DS-, and A4-SL-LNPs also exhibited appreciable accumulation in the white pulp, a compartment rich in T cells and DCs (Figure 5J,M).[68,69] In contrast, ALC-0315-LNPs showed weaker and more diffuse splenic signals. In lymph nodes, formulation-dependent localization patterns were observed across distinct anatomical compartments. A3-SS- and A4-SM/SL-LNPs were primarily detected in the medulla, which is enriched in medullary DCs, NK cells, and macrophages,[70−72] whereas A3-SM/SL-, A3-DL-, A4-SL-, and ALC-0315-LNPs were predominantly localized within the medullary sinuses. Within the medulla at the microanatomical level, A3-SL-, A3-DM-, and ALC-0315-LNPs exhibited comparable Raman signal intensities, while A3-DS-LNPs showed relatively lower accumulation (Figure 5K,M).

In the liver, which plays a central role in LNP clearance and gene delivery,[73,74] Raman imaging indicated that A3-SM- and A3-DL-LNPs were mainly localized around hepatic blood vessels, consistent with uptake by Kupffer cells.[75,76] Minimal signal from A3-SM-, A3-DL-, and A4-SM-LNPs within hepatocytes suggested limited endocytosis by parenchymal cells, indicating reduced hepatocyte tropism relative to ALC-0315. A3-SM-LNPs exhibited weak signals across all examined organs, consistent with rapid degradation or clearance. In contrast, A4-SS-LNPs displayed the strongest overall Raman signal and were broadly distributed between hepatic blood vessels and hepatocytes (Figure 5L,M).

To further assess the persistence of LNP biodistribution at the organ level, A3-DM-LNPs, A3-DL-LNPs, and ALC-0315-LNPs were labeled with the near-infrared fluorophore DiR and intravenously administered. Whole-body fluorescence imaging was performed at 2, 6, and 24 h postinjection, followed by ex vivo fluorescence imaging and quantitative analysis of major organs and lymph nodes at 24 h (Figure S37B−E). Time-resolved imaging revealed that A3-DM- and A3-DL-LNPs exhibited sustained organ-level signal retention over 24 h, whereas ALC-0315-LNPs showed more rapid redistribution and clearance (Figure S37B). Quantitative ex vivo analysis further demonstrated significantly higher accumulation of A3-DM/DL-LNPs in the spleen and lymph nodes compared with ALC-0315-LNPs at 24 h, while ALC-0315-LNPs predominantly localized to the liver (Figure S37C−E).

Together, Raman spectral imaging and time-resolved DiR fluorescence biodistribution provide complementary insights into the in vivo fate of the LNP formulations. Raman imaging reveals lipid chemistry-dependent spatial localization at the level of organ microarchitecture (Figure 5), while DiR fluorescence enables temporal and quantitative comparison of organ- and lymph node-level accumulation (Figure S37B−E). Collectively, these data indicate a sustained and formulation-dependent enrichment of A3-DM- and A3-DL-LNPs in immune organs, particularly the spleen and lymph nodes, relative to ALC-0315-LNPs, establishing a physicochemical basis for evaluating how lipid-level disposition correlates with downstream RNA delivery and immunotherapeutic outcomes.

https://doi.org/10.1021/jacs.5c23209
J. Am. Chem. Soc. XXXX, XXX, XXX−XXX

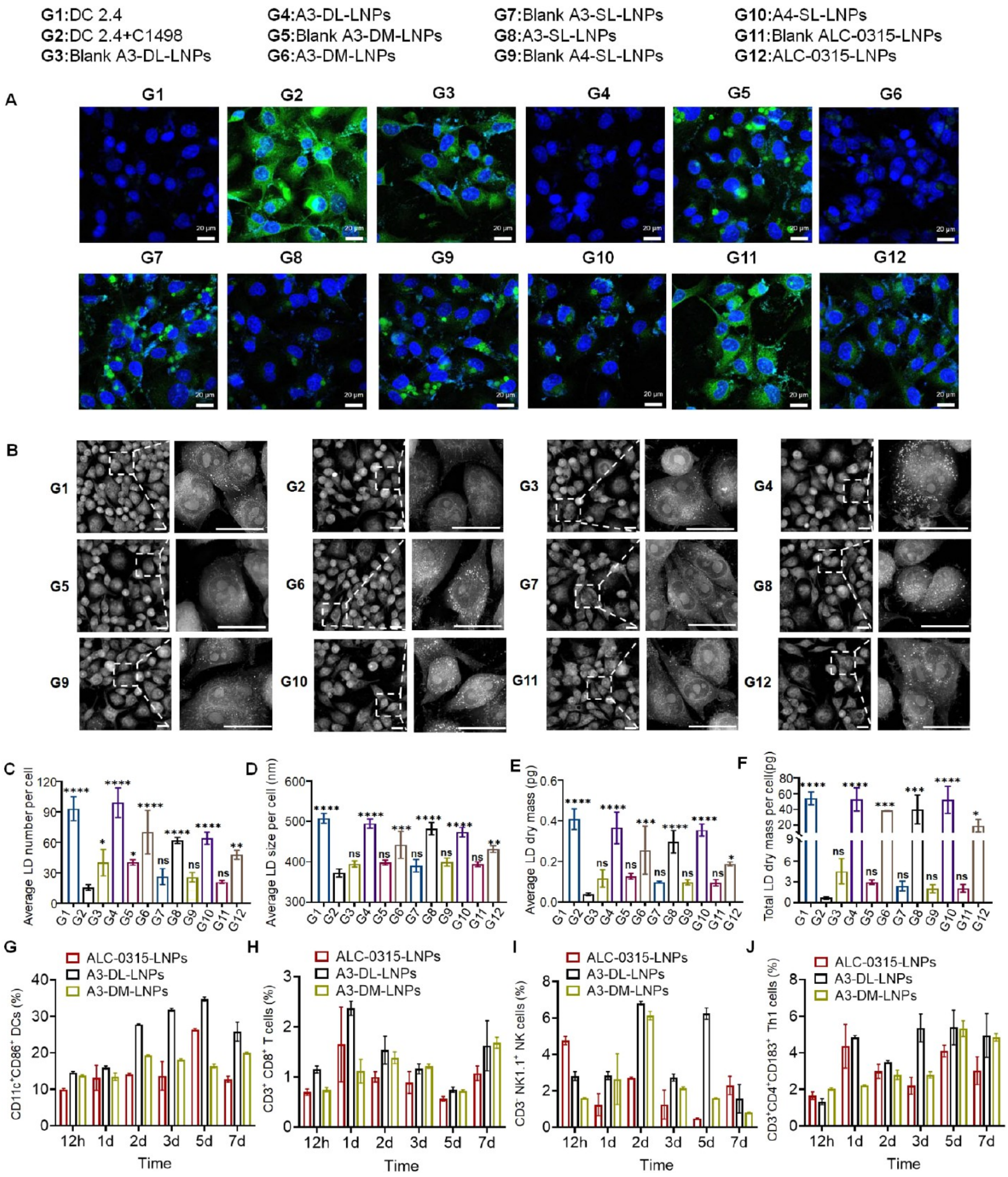

Figure 6. Potent in vitro and in vivo immune-regulatory effects of LNPs by codelivering siSTAT3 and OVA mRNA. (**A**) CLSM images showing thioflavin T fluorescence intensity as an indicator of ER stress in DC2.4 cells under different LNP formulation treatments. (**B**) Holotomographic imaging of lipid droplets in DC2.4 cells following various LNP formulation treatments. Scale bar, 20 μm. (**C−F**) Quantitative analysis of lipid droplet parameters, including size, number, and volume. (**G−J**) Long-term immune activation profiles in the spleen, as reflected by the percentage of: CD11c$^+$ CD86$^+$ activated DCs, CD3$^+$ CD8$^+$ cytotoxic T cells, CD3$^-$ NK1.1$^+$ NK cells, CD3$^+$ CD4$^+$ CD183$^+$ Th1 cells measured at 12 h, 1-day (1d), 2-day (2d), 3-day (3d), 5-day (5d), and 7-day (7d) post-treatment with A3-DM-LNPs, A3-DL-LNPs, and ALC-0315-LNPs (n = 3 per group). Statistical analysis was performed using one-way ANOVA. Significance levels: ns, not significant; *P < 0.05, **P < 0.01, ***P < 0.001, and ****P < 0.0001.

Immune Organ-Targeted Delivery of siSTAT3 and mRNA by A3-DL-LNPs for AML Treatment

Given the sustained and immune-organ−biased lipid distribution of A3-DM- and A3-DL-LNPs revealed by compartment-resolved Raman imaging and time-resolved in vivo biodistribution analyses, we next evaluated whether this carrier-level targeting translated into enhanced functional delivery of mRNA and siSTAT3 to the spleen and draining lymph nodes in vivo. The optimal outcomes of immunotherapies are achieved through the transfected mRNA to immune organs and triggering a robust immune response after the biodistribution behavior of LNPs.[77,78] To evaluate the delivery efficiency of mRNA to immune organs, we intravenously administered eGFP mRNA-LNPs based on nine imidazole-based bipolar ionizable lipids to C57BL/6J mice, using ALC-0315-LNPs as the positive control. The spleen, blood and draining lymph nodes including cervical, axillary, inguinal and popliteal from the left (L) and right (R) sides were then collected at 24 h post administration and analyzed by flow cytometry. Heatmaps depicted the mean normalized value for eGFP$^+$ expressing cells and immune cell populations corresponding to each LNP formulation in immune organs and peripheral blood samples, respectively (Figure 5N). A3-DS/DM/DL-LNPs achieved superior mRNA delivery in the spleen relative to ALC-0315-LNPs, which displayed more off-target expression. Notably, A3-DL and A4-SS-LNPs induced robust expression across most draining lymph nodes, while other formulations showed weaker signals. A3-DL-LNPs were particularly effective, achieving 8.4-fold and 1.6-fold higher eGFP expression in the spleen and lymph nodes, respectively, compared to ALC-0315-LNPs. Furthermore, distinct lymph node-specific expression patterns were observed, such as A3-SS/SM/SL/DM in the left cervical and A4-SM/SL in the axillary nodes, suggesting LNP formulation-dependent expression dynamics.

The enhancement in splenic transfection can potentially influence in vivo immune engineering.[79,80] Next, to assess the LNP-induced immune response, we evaluated specialized immune cell subsets in the spleen, lymph nodes and blood, respectively (Figure 5N). With the exception of A4-SM-LNPs, the remaining eight LNPs exhibited a significantly increased frequency of DC populations in the spleens relative to ALC-0315-LNPs. Meanwhile, A3-DS/DM/DL-LNPs promoted the proportion of both DCs, B cells and T cells in the spleens. The frequency of the antigen-presenting cells (APCs) in the A3-DM-LNP-treated group were 3.6-fold that in the ALC-0315-LNP-treated group. In comparison to ALC-0315-LNPs, the B cell frequencies demonstrated 7.2-, 8.9-, and 5.8-fold increases after treatment with A3-DS, A3-DM and A3-DL-LNPs, respectively. Similarly, the increase was 3.0-, 3.9-, and 5.9-fold after treatment with A3-DS, A3-DM and A3-DL-LNPs, respectively, in terms of CD8$^+$ T cell frequencies compared with ALC-0315-LNPs. Furthermore, higher numbers of APCs, DCs, B cells, and T cells were observed in lymph nodes from the mice treated with A3-DS/A3-DM/A3-DL-LNPs, whereas no such enrichment effect was detected in mice treated with ALC-0315-LNPs. These results suggested A3-DS/DM/DL-LNPs has the potential to elicit and maintain protective immunity in the immune organs like the spleen and lymph nodes against the AML progress. Compared to the ALC-0315-LNP-treated group, A3SS/SM/SL-LNPs induced an increase in the numbers of DCs and B cells. Meanwhile, it is found that compared to ALC-0315-LNP-treated group, A4SS/SM/SL-LNPs induce a moderate increase in the number of APCs, DCs and CD8$^+$ T cells, but there was no significant change in B cells. NK cell populations remained unchanged across all formulations. These data confirmed that the imidazole-based LNPs, particularly A3-DM/DL-LNPs, exhibited efficient transfection of immune organs and elicited potent immune responses following systemic administration. Notably, transfection efficacy did not strictly correlate with overall LNP tissue distribution (Figure 5J−N), implying that cellular uptake dynamics and LNP disassembly rates play critical roles. Indeed, mRNA expression in immune tissues was closely associated with plasma membrane affinity of the imidazole-based lipids (Figure 4E), underscoring the importance of lipid chemistry in determining transfection outcomes.

Regulation of Antigen-Presenting Functionality of DCs by STAT3 Silencing

Leukemia-derived inflammation and endoplasmic reticulum (ER) stress are known to impair the function of immune cells and compromise mRNA-encoded antigen presentation.[81,82] The pro-inflammatory immune microenvironment in acute myeloid leukemia (AML) contributes to disease progression and immune evasion, primarily through activation of the JAK/STAT pathway.[83,84] Concurrently, ER stress has been shown to induce STAT3 overactivation and dysregulate lipid droplet (LD) biogenesis in DCs, which disrupts antigen cross-presentation.[85,86] Therefore, it is critical to investigate whether small interfering RNA-mediated silencing of STAT3 (si-STAT3) in DCs can restore stable mRNA antigen presentation and reprogram T cell responses to mount durable immunity against AML.

In the evaluation of ER stress and lipid droplet dynamics, all LNP formulations were labeled with FITC and loaded with siSTAT3; formulations without siRNA were designated as blank LNPs. In vitro, DC2.4 cells cocultured with leukemia-derived C1498 cells exhibited a marked increase in thioflavin T-positive aggresomes, indicating elevated misfolded protein accumulation consistent with ER stress. Compared to A3/A4-SL-LNPs and ALC-0315-LNPs, treatment with A3-DM/DL-LNPs (G4 and G6) featuring a distinctive “M-shaped” architecture, significantly alleviated ER stress (Figure 6A). Utilizing a label-free holotomography (HT) imaging approach, we systematically investigated and quantitatively analyzed the biophysical parameters of lipid droplets in intact DC2.4 cells. The HT images provided three-dimensional and high-resolution refractive tomograms of DC2.4 cells, enabling precise segmentation of LDs based on their higher refractive index (RI) values compared with other subcellular organelles (Figure 6B).[87] Quantitative analysis demonstrated that coculture with C1498 cells significantly reduced key LD parameters in DC2.4 cells compared to healthy controls, with average number, size, LD dry mass, and total LD dry mass decreasing by ∼83%, 27%, 90%, and 99%, respectively (Figure 6C−F). Notably, treatment with A3-DL-LNPs significantly rescued the biophysical parameters of LDs in DC2.4 cells cocultured with C1498 cells, restoring them to healthy control levels, which attributed to the increased uptake efficiency of A3-DL-LNPs in DC2.4 cells (Figure S38).

To assess the functional consequence of STAT3 silencing on antigen presentation, we loaded A3-DL-LNPs with siSTAT3 and ovalbumin (OVA) mRNA as a model antigen and analyzed DC activation. The proportion of CD11c$^+$CD80$^+$CD86$^+$ DCs in the A3-DL-LNPs group was 1.37-fold higher than that of the PBS group. In addition, A3-DL-LNPs resulted in 1.51-fold higher MHC II expression than the PBS group (Figure S39). The bromodeoxyuridine (BrdU) incorporation was performed to evaluate the proliferation capability of the immune cells. Notably, the A3-DL-LNPs significantly elevated the proportion of BrdU$^+$CD3$^+$ T cells, BrdU$^+$CD3$^+$CD8$^+$ T cells, BrdU$^+$CD3$^-$CD49b$^+$ NK cells, and BrdU$^+$CD3$^+$CD4$^+$CD183$^+$ Th1 cells as compared to the PBS group, blank A3-DL-LNP group and A3-DL-LNP-siNC group (Figure S40). These effector and memory-forming populations are critical for mRNA vaccine-driven anti-AML immunity, enabling tumor cell elimination and durable protective immunity.

Furthermore, A3-DL-LNP treatment markedly increased the frequencies of CD3$^+$CD4$^+$IFN-γ^+ T cells, CD3$^+$CD4$^+$CD183$^+$IFN-γ^+ Th1 cells, CD3$^+$CD8$^+$IFN-γ^+ T cells, and CD11c$^+$IFN-γ^+ DCs by 112.42%, 104.58%, 57.8%, and 210%, respectively, over PBS-treated controls (Figure S41). Antigen presentation efficacy was confirmed by enhanced surface expression of the SIINFEKL-H2Kb complex

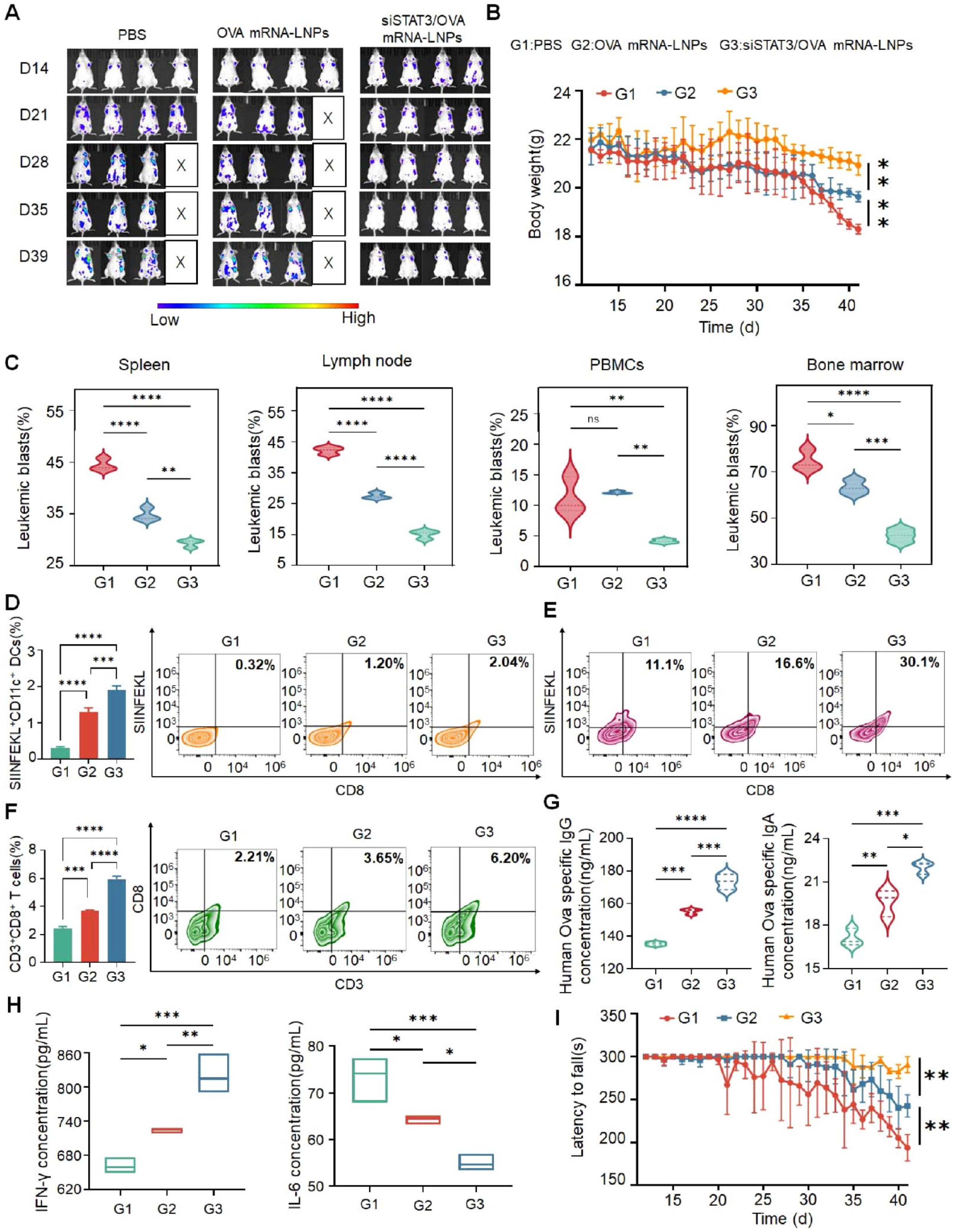

Figure 7. Antileukemic effects of siSTAT3/OVA mRNA-LNPs formulated with A3-DL ionizable lipid in a humanized GFP-positive HL-60-engrafted xenograft model. (**A**) Fluorescence imaging of humanized NSG mice engrafted with GFP-positive HL-60 cells, showing tumor burden on day 14, 18, 21, 25, 28, 32, 35, and 39 postengraftment. (**B**) Comparison of body weight changes across treatment groups. (**C**) Violin plots depicting the frequency of leukemic blasts ($GFP^+/CD45^+$) as a percentage of live cells in spleen, lymph node, peripheral blood, and bone marrow at the experimental end point. (**D**−**F**) Representative flow cytometry plots and quantitative analyses of $SIINFEKL^+$ $CD11c^+$ DCs, $SIINFEKL^+$ $CD3^+$ $CD8^+$ T cells, and $CD3^+$ $CD8^+$ T cells in spleen following different treatments ($n = 3$). (**G**) ELISA quantification of serum OVA-specific IgG and IgA antibody levels from each group ($n = 3$). (**H**) Plasma concentrations of IFN-γ and IL-6 measured by ELISA ($n = 3$). (**I**) Latency to fall assessed

Figure 7. continued

by the accelerating rotarod test ($n = 3$), evaluating motor coordination and balance. Statistical analysis was performed using one-way ANOVA. Significance levels: ns, not significant; $*P < 0.05$, $**P < 0.01$, $***P < 0.001$, and $****P < 0.0001$.

on CD11c$^+$ DCs, demonstrated by a 1.82-fold increase in SIINFEKL$^+$ DC frequency and a 12.95-fold increase in mean fluorescence intensity (MFI) versus the siNC control (Figure S42A,B). In turn, these DCs drove potent antigen-specific T cell responses, with SIINFEKL-specific CD8$^+$ and CD4$^+$ T cells increased by 32.16-fold and 18.04-fold, respectively (Figure S42C,D). These findings establish STAT3 silencing as a key factor in enhancing antigen presentation and T cell priming to promote antileukemia therapeutic efficacy. Accordingly, in the transwell coculture system, splenic lymphocytes seeded in the apical chamber exhibited significantly increased IFN-γ secretion following priming by A3-DL-LNP-treated DCs, which correlated with enhanced cytotoxicity against leukemic C1498 cells in the basal chamber (Figures S43 and S44). These findings indicate a dual mechanism of action of siSTAT3 and mRNA delivery via A3-DL-LNPs involving both immune activation and direct antitumor effects.

To evaluate long-term immune activation, we assessed immune cell populations in vivo following systemic administration of A3-DM-LNPs, A3-DL-LNPs and ALC-0315-LNPs with encapsulation of OVA mRNA and siSTAT3, respectively. On Day 7 postinjection, the A3-DL-LNP group showed 2.0-fold, 1.5-fold, and 1.6-fold higher frequencies of splenic DCs, T cells, and Th1 cells, respectively, compared to the ALC-0315-LNP group (Figure 6G−J). Additionally, DCs and T cells in lymph nodes, and DCs, Th1 and NK cells in PBMCs, were significantly elevated in A3-DL-LNP-treated mice and remained elevated through Day 7 (Figures S45 and S46), reflecting a sustained systemic antileukemic immune response.

In Vivo Efficacy Study in the Orthotopic AML Mouse Model

To address the limitations posed by interspecies differences between murine and human immune systems, we established a humanized cell line-derived xenograft (PBMC-CDX) model to evaluate the antileukemic efficacy of A3-DL-LNPs. Human peripheral blood mononuclear cells (PBMCs) that derived from an HLA-A*0201$^+$ healthy donor were engrafted into NOD-SCID IL2Rγ^-/$^-$ (NSG) mice to reconstitute a functional human immune system. Two weeks later, the NSG mice were administrated with busulfan via intraperitoneal injection. After 24 h, these humanized mice were inoculated intravenously with HL-60 cells stably expressing GFP and luciferase. Fourteen days post-tumor challenge, mice were vaccinated intravenously with different LNP formulations, and therapeutic outcomes were systematically assessed. AML progression was monitored in real-time using in vivo bioluminescence imaging (Figure 7A). The PBS-treated group exhibited rapid systemic AML dissemination, reflecting high disease aggressiveness. A modest reduction in tumor burden was observed in mice treated with OVA mRNA-LNPs alone, indicating limited efficacy of antigen-only mRNA vaccination. In contrast, codelivery of OVA mRNA and siSTAT3 via A3-DL-LNPs resulted in a marked suppression of AML progression and maintenance of stable body weight throughout treatment (Figure 7B). Given the preferential biodistribution of A3-DL-LNPs to the spleen and lymph nodes, this dual-delivery strategy effectively stimulated the humanized immune system. Notably, siSTAT3/OVA mRNA-LNP treatment significantly reduced the frequency of leukemia blasts in the spleen and lymph nodes by 34.0% and 64.4%, respectively, compared with PBS controls. Furthermore, leukemia burden in peripheral blood and bone marrow was reduced by 62.4% and 43.2%, respectively (Figure 7C). These reductions likely reflect enhanced immune cell trafficking from lymphoid tissues to the bone marrow, contributing to improved clearance of leukemic blasts in the marrow niche.[88,89] Hematoxylin and eosin (H&E) staining of spleen sections corroborated the antileukemic efficacy of the siSTAT3/OVA mRNA-LNP treatment, demonstrating histological evidence of reduced leukemogenesis group (Figure S47).

siSTAT3/OVA mRNA-LNPs Enhance Antigen Presentation and Elicit Potent Immune Responses

Inhibiting STAT3 activity within peripheral immune organs presents a promising strategy to restore LD homeostasis, alleviate ER stress, and enhance antigen presentation, thereby improving DC and T cell activation and boosting the therapeutic efficacy of mRNA vaccines (Figure 6).[11] To evaluate the sustained cellular immune responses induced by this approach, flow cytometry was conducted on spleen and lymph node samples following treatment with siSTAT3/OVA mRNA-LNPs. We first assessed the activation of DCs by quantifying CD11c$^+$ CD80$^+$, CD11c$^+$ CD86$^+$, and CD11c$^+$ CD80$^+$ CD86$^+$ DC populations. These activated DC subsets were significantly elevated in the spleens of mice treated with siSTAT3/OVA mRNA-LNPs compared to those receiving OVA mRNA-LNPs or PBS (Figure S48), with similar trends observed in lymph nodes (Figure S49). To further characterize antigen presentation, we measured SIINFEKL$^+$ CD11c$^+$ DCs and MHC molecule expression. In the spleen, siSTAT3/OVA mRNA-LNPs enhanced the frequencies of SIINFEKL$^+$ CD11c$^+$, MHC-I$^+$ CD11c$^+$, and MHC-II$^+$ CD11c$^+$ DCs by 45.7%, 131.1%, and 46.7%, respectively, relative to the OVA mRNA-LNP group (Figures 7D and S50). These results demonstrate that STAT3 inhibition effectively reverses antigen presentation deficiencies and mitigates immunosuppression. Comparable increases were also observed in lymph nodes (Figure S51). The elevated presence of SIINFEKL-MHC I/II complexes on DCs is critical for priming antigen-specific cytotoxic CD8$^+$ T cells.[90] Accordingly, the proportion of SIINFEKL$^+$ CD3$^+$ CD8$^+$ T cells increased by ∼1.7-fold in the spleen and ∼2.2-fold in lymph nodes in the siSTAT3/OVA mRNA-LNP group compared to the OVA mRNA-LNP group, indicating efficient T cell priming and potential leukemic cell killing (Figures 7E and S52). Furthermore, siSTAT3/OVA mRNA-LNPs significantly increased CD3$^+$ CD4$^+$ CD183$^+$ Th1 cell frequencies in both spleen and lymph nodes, thereby enhancing CD8$^+$ T cell-mediated antitumor responses (Figure S53).[91] This was accompanied by a robust elevation in CD3$^+$ CD8$^+$ T cells in both organs, demonstrating their superior cytotoxic effects against leukemia cells (Figures 7F and S54). Taken together, these data confirm that siSTAT3/OVA mRNA-LNPs induce potent, antigen-specific cellular immunity in the humanized AML model. Notably, the memory T cell marker CD62L was significantly upregulated in both spleen and lymph nodes. CD62L$^+$ memory T cell populations increased by ~4.7-fold and 1.9-fold over PBS and OVA mRNA-LNP groups in the spleen, and by ~2.6-fold and 1.9-fold in lymph nodes, respectively, highlighting the establishment of long-term immunological memory (Figure S55).

Given the known association between STAT3 overexpression and NK/NKT cell dysfunction in AML patients,[92] we also analyzed these populations. The proportion of CD3$^-$ CD56$^+$ NK cells increased by ~1.6-fold and ~1.8-fold in the spleen and lymph nodes, respectively, following siSTAT3/OVA mRNA-LNP treatment (Figure S56). Additionally, the frequencies of CD3$^+$ CD56$^+$ NKT cells were significantly elevated in both the spleen and lymph nodes in the siSTAT3/OVA mRNA-LNP group compared to the PBS group. In contrast, no significant change in NKT cell populations was observed in the spleen of the OVA mRNA-LNP group (Figure S57). To assess systemic immunity, PBMCs were analyzed. Flow cytometry revealed enhanced frequencies of DCs, T cells, Th1 cells, and NK cells in the bloodstream of mice treated with siSTAT3/OVA mRNA-LNPs, confirming robust systemic immune activation and immune cell trafficking (Figures S58–S61). Finally, humoral responses were evaluated 4 weeks after a single vaccine dose. Mice treated with siSTAT3/OVA mRNA-LNPs exhibited significantly higher serum levels of anti-OVA IgG, with notable increases in IgA, IgM, IgG1, and IgG2c isotypes, compared to both PBS and OVA mRNA-LNP groups (Figures 7G and S62). The expansion of Th1 cells likely promoted B cell activation, leading to enhanced antibody production, cytokine secretion, and antigen presentation functions.[93,94] These antibodies, in turn, can enhance T cell responses and potentiate NK cell-mediated cytotoxicity.

In addition to siSTAT3/OVA mRNA-LNPs, a comparison between the efficacy of A3-DL-LNPs and ALC-0315-LNPs was performed in the same humanized HL-60 xenograft model. As shown in Figures S63 and S64, A3-DL-LNPs demonstrated superior therapeutic effects, correlating with enhanced immune responses and better tumor control compared to ALC-0315-LNPs. Specifically, A3-DL-LNPs led to greater T cell activation, more robust immune responses, and higher frequencies of cytotoxic T cells, NK cells, and mature DCs, ultimately resulting in reduced leukemic cell populations and better therapeutic outcomes.

Mouse Behavior Analysis after Vaccination

As acute myeloid leukemia (AML) progresses, patients often develop frailty syndrome, characterized by low physical activity and diminished functional status. This decline is associated with poor performance status, reduced quality of life, and worse clinical outcomes, and is often linked to abnormal cytokine profiles, including low levels of IFN-γ and elevated levels of IL-6 in serum.[94,95] In this study, treatment with siSTAT3/OVA mRNA-LNPs led to significant modulation of cytokine expression, restoring IFN-γ levels and reducing IL-6 levels by 23.5% and 26.3%, respectively, compared to the PBS control group. These changes contributed to an improvement in the physiological and locomotor status of the treated mice, as evidenced by the codelivery of siSTAT3 and OVA mRNA (Figure 7H). To assess the impact of the treatments on locomotor coordination, we performed the rotarod test, which measures both the duration mice remain on the rotating rod and their speed upon falling (Figures 7I and S65). Mice in the PBS group exhibited significant locomotor deficits, as indicated by a decreased latency to fall at the accelerated speed mode. On Day 30, the time spent on the rod was reduced by 35.5% compared to Day 1 in the PBS group, and by 19.1% in the OVA mRNA-LNP group. In contrast, mice treated with siSTAT3/OVA mRNA-LNPs showed minimal reduction in latency to fall, demonstrating preserved locomotor coordination and significant therapeutic benefits. In conclusion, the siSTAT3/OVA mRNA-LNP treatment effectively ameliorates both the cytokine imbalance and locomotor deficits associated with AML, showing potent antileukemic effects and improving overall physical and functional status in vivo.

Assessing In Vivo LNP Toxicity

Given the potent immune activation and modulation of endothelial tight junctions observed for the LNP formulations, a systematic evaluation of their in vivo tolerability and potential organ toxicity was conducted. The lipid dose was based on encapsulation of 0.5 mg/kg mRNA, corresponding to a total lipid dose of 3 mg/kg, with a high-dose group set at twice this level for toxicity assessment. At the lower dose, most LNP formulations, including A3-DS/DM-LNPs, A3-SS/SM-LNPs, and A4-SS/SM/SL-LNPs, exhibited alanine aminotransferase (ALT) levels comparable to baseline values observed in untreated mice (ALT ≈ 3 U/L). In contrast, A3-DL-LNPs, SM-102-LNPs, ALC-0315-LNPs, and MC3-LNPs showed relatively elevated ALT levels. At the higher dose, ALT levels for A3-DM-LNPs (6.23 U/L) and A3-DL-LNPs (8.87 U/L) remained lower than those observed for the FDA-approved ALC-0315-LNPs (13.42 U/L) (Figure S66A). Alkaline phosphatase (ALP) levels followed trends similar to those of ALT. At the lower dose, A3-DM-LNPs and A3-DL-LNPs displayed ALP levels close to baseline values. At the higher dose, a modest increase in ALP was observed for A3-DM-LNPs, indicating a mild dose-dependent elevation, though values remained lower than those measured for ALC-0315-LNPs (Figure S66B). For aspartate aminotransferase (AST), at the lower dose, A3-DS-LNPs, A3-DL-LNPs, and A3-SM-LNPs exhibited lower AST levels relative to SM-102-LNPs, ALC-0315-LNPs, and MC3-LNPs, which showed more pronounced elevations. Across imidazole-based formulations, AST values consistently remained lower at the lower dose, indicating reduced hepatic enzyme perturbation under these conditions (Figure S66C).

In addition to liver function, renal tolerability was assessed by measuring serum creatinine and blood urea nitrogen (BUN) levels. At the lower dose, creatinine levels for most formulations, including A3-DM-LNPs and A3-DL-LNPs, remained close to baseline values (~135 μmol/L), indicating minimal impact on renal function. At the higher dose, creatinine levels for A3-DM-LNPs and A3-DL-LNPs were comparable to those observed for SM-102-LNPs and ALC-0315-LNPs (Figure S66D). Similarly, BUN levels for A3-DM-LNPs and A3-DL-LNPs remained stable and comparable to clinically used LNP formulations at the higher dose (Figure S66E).

Furthermore, gross and histological examinations of major organs were performed to further assess in vivo tolerability. Representative H&E-stained sections of the liver, spleen, and kidney did not reveal overt pathological abnormalities following administration of A3-DM/DL-LNPs at either the low or high dose (Figure S67). Specifically, no obvious signs of hepatocellular necrosis, inflammatory cell infiltration, splenic architectural disruption, or renal tubular damage were observed under the experimental conditions employed. To assess acute systemic immune activation, serum levels of IL-6 and TNF-α were measured 4 h after intravenous administration of A3-DM-LNPs, A3-DL-LNPs, or ALC-0315-LNPs at a total lipid dose of 3 mg/kg. No significant cytokine elevation was observed for the imidazole-based LNPs compared to ALC-0315-LNPs (Figure S68). Collectively, these results indicate that imidazole-based A3-DM/DL-LNPs exhibit acceptable liver and kidney tolerability within the tested dose range.

■ DISCUSSION

The rational design of LNPs plays a critical role in optimizing their ability to deliver nucleic acid therapeutics, such as mRNA and siRNA, to specific target tissues and cells. This study explores a series of imidazole-based bipolar ionizable lipids and their potential for codelivering mRNA and siRNA in the treatment of AML. Achieving efficient RNA encapsulation, targeted delivery, and therapeutic activity requires LNPs with optimized structural properties, a central challenge in the development of RNA-based therapeutics. In this study, we propose a structure−property-activity framework that connects lipid molecular architecture to LNP internal organization, membrane interactions, intracellular trafficking, and ultimately, therapeutic efficacy (Scheme 1).

The internal structure of LNPs is crucial for determining their functionality. The T-S model fitting in our study allows us to quantify mesophase disorder without assuming a specific lattice model, providing a more accurate structural representation of these LNPs. Specifically, bipolar imidazole-based lipids, such as A3-DM and A3-DL, exhibit disordered multicompartment architectures with quasi-periodic nanostructures, as shown by SAXS and cryo-TEM (Figures 3B−C and S24). The distinct peak observed at the 0.9−1.0 nm^{-1} q range in imidazole-based LNPs (A3-DM/DL) appeared at a lower q-value than that of the benchmark ALC-0315-LNPs (~1.25 nm^{-1}), indicating a more fluidic and less constrained packing of nucleic acids. This enhanced fluidity likely improves RNA encapsulation and transfection efficiency. Moreover, such an internal architecture provides structural flexibility and spatial heterogeneity, enabling the simultaneous accommodation of rigid siRNA and flexible mRNA while maintaining membrane integrity during cellular uptake (Figure 2E−F).

We observed a correlation between the multicompartmental morphology and surface conformation of imidazole-based LNPs and their transfection efficiency, cellular uptake, biodistribution, and therapeutic efficacy. At the molecular level, this behavior can be rationalized by considering the conformational adaptability of the piperazine-based polar headgroup. Previous studies have shown that piperazine-containing frameworks exhibit pronounced structural plasticity, allowing their geometry to reorganize in response to steric constraints and substitution patterns.[96−99]

In the present lipid design, the piperazine ring is flanked by two imidazole moieties and further constrained by hydrophobic alkyl chains of increasing length. Such a molecular environment is expected to promote nonplanar conformational rearrangements of the piperazine core, giving rise to the observed "M-shaped" polar headgroup geometry.[96] This conformational reorganization effectively enlarges the polar headgroup cross-sectional area while enabling the attachment of four alkyl chains, thereby increasing the effective hydrophobic tail volume and introducing intrinsic curvature frustration that disfavors classical lamellar bilayer formation and instead favors bicontinuous membrane organization (Figures 3A, S15 and S16). From a soft-matter perspective, the combined increase in hydrophobic tail volume and headgroup cross-sectional area shifts the effective packing behavior toward regimes associated with negative curvature and nonlamellar assemblies. Consistent with this interpretation, A3-DM/DL-LNPs, with their multicompartment architecture, exhibit significantly stronger membrane-binding affinity at physiological pH compared to ALC-0315-LNPs (Figures 4E−G and S30), correlating with enhanced membrane interaction, cellular uptake, transfection efficiency, and improved therapeutic outcomes (Figures 2C−F and 4A). By contrast, lipids with more linearized headgroup configurations, such as A3-SS/SM/SL and A4-SS/SM/SL (Figures 3A and S18−S23), lack this curvature frustration, resulting in less heterogeneous internal structures and diminished delivery performance, underscoring the structure-dependent nature of the observed self-assembly behavior.

Additionally, A3-DM/DL-LNPs demonstrated reduced membrane affinity at acidic pH, which helps avoid lysosomal sequestration, enhancing intracellular trafficking via caveolae-mediated endocytosis and promoting cytosolic RNA release. This mechanism not only reduces lysosomal degradation but also improves the overall therapeutic response, particularly in cancer therapies where immune modulation and efficient antigen presentation are essential. In contrast, the piperazine moieties in A3-SS/SM/SL and A4-SS/SM/SL formulations occupy the hydrophilic domain ahead of the dihydroimidazole group, resulting in a more linear molecular architecture, which correlates with lower membrane interaction and reduced delivery efficiency (Figures 3A, S18−S23 and S30). Importantly, A3-DM/DL-LNPs preferentially engage caveolae-mediated endocytosis, bypassing the lysosomal pathway and ensuring rapid RNA release, a process that contrasts with the acid-triggered endosomal escape mechanism seen in ALC-0315-LNPs (Figures S32 and S33).

In vivo, we employed Raman spectroscopy imaging to correlate the spatial localization of ionizable lipids with RNA expression patterns (Figure 5), offering insights into the long-term immune response influenced by the in vivo fate of the LNPs. A3-DM/DL-LNPs preferentially accumulated in the spleen and lymph nodes, which are rich in immune cells such as dendritic cells (DCs), B cells, and T cells. This targeted distribution is crucial for optimizing immune responses, as it ensures efficient delivery to immune-rich tissues, facilitating RNA antigen presentation and activating the immune system effectively.

In the context of AML, dysregulated antigen processing in DCs, characterized by incomplete maturation, poor antigen loading, and phenotypic heterogeneity, contributes to T cell exhaustion.[100] Single-cell profiling of AML patients reveals that chemotherapy induces a pronounced expansion of exhausted T cells, which is a key driver of chemotherapeutic resistance.[101] Despite the clinical adoption of various immunotherapies, including monoclonal antibodies, bispecific antibodies, CAR-T cell therapy, and immune checkpoint inhibitors, T-cell exhaustion remains a significant barrier to treatment efficacy.[102] STAT3 signaling blockade has shown promise in rescuing DC functionality and promoting effector T-cell activation,[103] providing a strategy to combat T-cell exhaustion and improve AML treatment outcomes. In our study, A3-DM/DL-LNPs codelivering mRNA and siSTAT3 effectively restored DC function, redirected T cell immunity, and enhanced the immune response to AML by silencing STAT3, mitigating ER stress, and modulating lipid droplet dynamics. This strategy combats T-cell exhaustion and induces a persistent immune response, leading to improved therapeutic outcomes (Figures 6A−F and 7).

In summary, our data establish a clear structure-property-activity relationship wherein bipolar imidazole-based lipids, through their "M-shaped" headgroups and multitail structures, dictate not only the internal architecture of the LNPs but also their surface properties and dynamic membrane interactions. These features enable efficient RNA encapsulation, enhanced cytosolic delivery, and optimized biodistribution, leading to significant therapeutic efficacy in AML models. The specific intracellular trafficking pathways further highlight the influence of molecular design on therapeutic outcomes, ensuring efficient mRNA delivery to immune organs and sustained immune responses in AML.

■ CONCLUSION

In this study, we have developed a series of imidazole-based multicompartment LNPs designed for the codelivery of mRNA and siSTAT3. These nanoparticles exhibit a unique "M-shaped" architecture, which facilitates enhanced membrane interaction, cellular uptake, and transfection efficiency. Structural characterization using cryo-TEM and SAXS, alongside functional data, reveals that these LNPs exhibit superior RNA encapsulation and efficient delivery, especially to immune organs such as the spleen and lymph nodes. The imidazole-based LNPs, particularly A3-DM and A3-DL formulations, promote enhanced antigen presentation in DCs, alleviate ER stress, and modulate immune responses, reversing T cell exhaustion in AML. Additionally, these LNPs induce potent antileukemic effects through both immune activation and direct cytotoxicity. Notably, the formulation-dependent enhancement in immune organ targeting and efficient transfection makes A3-DM/DL-LNPs a promising platform for RNA-based therapies in AML. Our findings emphasize the critical role of lipid molecular design in optimizing RNA delivery and immune modulation for enhanced therapeutic outcomes.

■ EXPERIMENTAL MATERIALS AND METHODS

Materials

8-Pentadecanone, 12-Tricosanone, 1-(3-Aminopropyl)-4-methylpiperazine, 4-(4-Methylpiperazin-1-yl)butan-1-amine, D-Luciferin sodium, Sodium 4,5,6,7-tetrachloro-2″,4″,5″,7″-tetraiodo-3-oxo-3H-spiro[isobenzofuran-1,9′-xanthene]-3′,6′-bis(olate) (Rose Bengal sodium) and 2-(4-(Dimethylamino)phenyl)-3,6-dimethylbenzo[d]-thiazol-3-ium chloride (Thioflavin T). Nystatin, LY294002, Fucoidan, and Chitosan were obtained from Bide Pharmatech Co., Ltd. (Shanghai, China). Heparin sodium salt, Busulfan, 4-Heptanone, Ethyl Isocyanoacetate, 1,4-Bis(3-aminopropyl)piperazine, Dynasore, Chlorpromazine, 5-(*N*-ethyl-*N*-isopropyl)amiloride (EIPA), and Methyl-β-cyclodextrin (MBCD) were purchased from Shanghai Aladdin Biochemical Technology Co., Ltd. (Shanghai, China). Granulocyte-Macrophage Colony Stimulating Factor (GM-CSF) was purchased from Nanjing GenScript Biotechnology Co., Ltd. (Nanjing, China). 1,2-Dimyristoyl-*sn*-glycero-3-phosphocholine (DMPC), 1,2-Dioleoyl-*sn*-glycero-3-phosphocholine (DOPC), 1,2-Dipalmitoyl-*sn*-glycero-3-phosphorylcholine (DPPC), and 1,2-Distearoyl-*sn*-glycero-3-phosphocholine (DSPC) were purchased from Shanghai Ponsure Biotech, Inc. (Shanghai, China). *N*-(Carbonyl methoxy polyethylene glycol 2000)-1,2-distearoyl-*sn*-glycerol-3-phosphoethanolamine, sodium salt (DSPE-mPEG2000) was purchased from Shanghai AVT Pharmaceutical Technology Co., Ltd. (Shanghai, China). Cholesterol was purchased from Sigma-Aldrich Co., Ltd. (St. Louis, MO, USA). Cy5-siRNA and siSTAT3 were purchased from General Biosystems Co., Ltd. (Anhui, China). Dialysis tubing (MWCO 30 kDa) was purchased from Viskase Companies, Inc. (Lombard, IL, USA). HiScript III first Strand cDNA Synthesis Kit (+gDNA wiper) and Taq Pro Universal SYBR qPCR Master Mix were obtained from Nanjing Vazyme Biotech Co., Ltd. (Nanjing, China). Lyso-Tracker Green, RiboGreen, HEPES, DAPI, and Annexin V-FITC/PI Staining Kit were purchased from Beyotime Institute of Biotechnology (Haimen, China). Chloroform-d and Deuterium oxide were purchased from Shanghai Macklin Biochemical Co., Ltd. (Shanghai, China). DNP-10 was purchased from Bruker Nano, Inc. (Billerica, MA, USA). Mica Discs were purchased from Ted Pella, Inc. (Redding, CA, USA). Collagen Type I was obtained from Beijing Solarbio Science & Technology Co., Ltd. FITC-cholesterol was purchased from Chongqing Yusi Pharmaceutical Technology Co., Ltd. (Chongqing, China). Amine-reactive second-generation (AR2G) biosensors were purchased from Forte Biosciences, Inc. (Dallas, TX, USA). 2-(*p*-toluidino)-6-naphthalenesulfonic acid (TNS) was purchased from Abcam (Shanghai) Trading Co., Ltd.

Cell Culture

DC 2.4, HL-60, and C1498 cell lines were purchased from Nanjing SenBeiJia Biological Technology Co., Ltd. (Nanjing, China). DC 2.4 and HL-60 cells were cultured in RPMI 1640 supplemented with 10% FBS and 1% penicillin/streptomycin at 37 °C, 5% CO_2, and 100% humidity. C1498 cells were cultured in Dulbecco's modified Eagle's medium (DMEM) supplemented with 10% FBS and 1% penicillin/streptomycin at 37 °C, 5% CO_2, and 100% humidity.

Synthesis of Imidazole-Based Ionizable Lipids

Imidazole-based lipids were synthesized via a modular three-component condensation reaction involving piperazine amines, alkyl ketones, and ethyl isocyanoacetate, as illustrated in Figure 1. Variation of the alkyl ketone and piperazine linker enabled systematic modulation of hydrophobic tail architecture and molecular symmetry. This reaction strategy is adapted from previously reported multi-component condensation reactions for imidazole formation.[104,105] Detailed experimental procedures and compound characterization are provided in the Supporting Information.

Preparation and Characterization of LNPs

LNPs were prepared by INano L/L+, a microfluidic device from Micro&Nano Biologics Co., Ltd. The siRNA and mRNA solution was loaded as the aqueous phase, and the organic phase was composed of ionizable lipid, helper lipid, cholesterol, and DSPE-PEG2000 in an appropriate amount of methanol and tetrahydrofuran. The complexation of aqueous and organic phases were facilitated by the small dragon micromixer within the microfluidic channels to form LNPs. These two solutions were displayed in two 15 mL centrifugal tubes and fed into the microfluidic device. After preparation, the residual organic solvent was removed by the dialysis tubing (MWCO 30 kDa). The encapsulation efficiency of siRNA and mRNA was evaluated by the RiboGreen assay. The size and polydispersity index (PDI) of the LNPs were measured by dynamic light scattering (DLS), and the morphology was observed with Cryo-Transmission Electron Microscopy (Cryo-TEM).

RNA Extraction and Real-Time qPCR

Total RNA of DC 2.4 was extracted using the RNeasy Animal RNA Isolation Kit (Beyotime) according to the manufacturer's protocol. RNA was then reverse transcribed using HiScript II first Strand cDNA Synthesis Kit, and qPCR was performed by Taq Pro Universal SYBR qPCR Master Mix in the LightCycler 480 (Basel, Switzerland). The mRNA levels were normalized with β-actin. The siSTAT3 sequence was sense strand 5′-CACCTTGGATTGAGAGTCAAGAC-3′, antisense 5′-AGGA-ATCGGCTATATTGCTGGT-3′ for mice and sense strand 5′-CAGCAGCTTGACAC-ACGGTA-3′, antisense 5′-AAA-CACCAAAGTGGCATGTGA-3′ for humans.

Synchrotron Small-Angle X-ray Scattering (SAXS)

The SAXS measurements were conducted at BL19U2 beamline of the National Facility for Protein Science Shanghai (NFPSS), located within the Shanghai Synchrotron Radiation Facility (SSRF). The incident X-ray beam was set to 12 keV, corresponding to a wavelength (λ) of 0.103 nm. Scattering profiles were recorded using a PILATUS3X 2M detector (Dectris, Switzerland). The sample-to-detector distance was set as 2675 mm, enabling a scattering vector q obtained from 0.07 to 4.5 nm^{-1}, where $q = 4\pi\sin\theta/\lambda$, with θ represents half of the scattering angle. Samples were pumped into a flow-through quartz capillary with an inner diameter of 1.5 mm to ensure consistent sample handling and minimize the background deviation. The exposure time was fixed at 1 s per scattering pattern, and 20 consecutive frames were collected and averaged to improve signal-to-noise ratio as well as assess the potential radiation stability. Primary data reduction, background subtraction and radial averaging, was performed using the BioXTAS RAW software package. The resulting 1-dimensional scattering profiles of imidazole-based LNPs were subsequently fitted using the Teubner−Strey model using SASfit software (version 0.94.12) with least-squares minimization.[50] In the T-S model, the SAXS intensity $I(q)$ is expressed as , where q is the scattering vector, A is a scaling factor related to contrast and volume fraction, I_{bg} is a constant background term, and a, b, and c are fitting parameters that describe the balance between interfacial tension and curvature elasticity of the internal domains.

From these parameters the characteristic domain spacing (d) reflects the dominant internal length scale and is given by $q_{max} = \sqrt{\frac{-c}{2b}}$, $d = \frac{2\pi}{q_{max}}$, representing the average distance between adjacent domains or interfaces but does not imply long-range periodic order.

The other structure parameter, correlation length (ξ), describes the spatial extent over which density fluctuations remain correlated and is calculated as $\xi = \sqrt{\frac{2b}{a - c^2/(4b)}}$. A larger ξ indicates stronger and more persistent internal correlations, whereas a smaller ξ reflects more disordered structures.

The real-space scales d-spacing of ALC-0315-LNPs was derived from scattering profile based on the Bragg's law as:[106] $q = \frac{2\pi}{d}$.

In Situ Determination of pK_a Using TNS

The apparent pK_a of LNPs was determined by fluorescent probe 2-(p-toluidino)-6-naphthalene sulfonic acid (TNS). TNS was prepared as a 100 μM stock solution in distilled water. The total lipids of LNPs were diluted to 100 μM in 90 μL of buffered solutions containing 10 mM HEPES, where the pH ranged from 2.5 to 12.0. Ten μL of TNS stock solution was added to the LNP solutions and mixed in the black 96-well plate. The fluorescence intensity was detected by ID5 Multi-Mode Microplate Readers (Molecular Devices) using excitation and emission wavelengths of 321 and 445 nm.

Live-Cell Fluorescence Imaging

Super-resolution imaging of lysosomal structures was performed using commercialized Polar-SlM (Airy Technology Co., Ltd., China). Images were acquired using a 100x/1.49 NA oil immersion objective (Nikon, Japan). 1 × 10^6 of DC 2.4 were seeded in 35 mm glass bottom dishes (Cellvis, D35-20-1.5-H) and maintained at 37 °C and 5% CO_2 in a humidified chamber for live SlM imaging. The 488 nm and 561 nm lasers were used to excite LysoTracker Red and FITC-labeled LNPs with 2D SIM modality. The SIM reconstruction process was conducted using the Airy-SIM software. After incubation of different LNPs with DC 2.4 for 3.5 h, the live-cell fluorescence imaging was recorded for a total of 5 min at intervals of 30 s.

Atomic Force Microscopy (AFM)

100 μL of LNP solution (5 mg/mL) was dropped onto the surface of the mica discs and incubated for 1 h at room temperature. Then the surface was washed 5 times with 100 μL of distilled water. AFM imaging was carried out in PeakForce Quantitative Nanomechanical Mapping (QNM) mode in fluid using a DNP10-C cantilever (silicon nitride, nominal stiffness: 0.24 N/m, tip radius: 20 nm; Bruker, USA). Prior to the measurements, the cantilevers were calibrated by using the thermal method in fluid. The cantilever moves toward the LNP from an out-of-contact area at zero force along the approach curve, down to the set point force position when the Z displacement is equal to zero, and followed by retracting to the full extension length of the displacement. The force−indentation curve was recorded during the process. All images of LNPs obtained from AFM were processed by the software NanoScope Analysis (Version 3.00, Bruker).

Holotomography

Three-dimensional (3D) holographic tomographic (HT) imaging was performed using Tomocube HT-X1 (Tomocube, Daejeon, Korea). 1 × 10^6 of DC 2.4 were seeded in 35 mm glass bottom dishes (Cellvis, D35-20-1.5-H), and the DC 2.4 were incubated with 5 × 10^5 of C1498 cells for 24 h to simulate the leukemia microenvironment. The changing process of LDs was monitored after incubation with different formulations for 24 h at 37 °C under a humidified atmosphere containing 98% air and 5% CO_2. The HT-X1 microscope, incorporating a Mach−Zehnder interferometer, was utilized for the three-dimensional RI tomographic reconstruction of the cells. LD quantification and volumetric analysis were performed using TomoAnalysis software (Version 2.1, Tomocube).

Endoplasmic Reticulum (ER) Stress Evaluation

1 × 10^6 of DC 2.4 were seeded in confocal dishes and incubated with 5 × 10^5 of C1498 cells for 24 h to simulate the leukemia microenvironment. After treated with different formulations for 24 h, cells were fixed in 4% paraformaldehyde, permeabilized with 0.1% Triton X, and washed with PBS for three times. Then cells were incubated with Thioflavin T (10 μM) for 20 min at 37 °C. Afterward, cells were washed with PBS, stained with DAPI, and observed by a confocal laser scanning microscopy (CLSM, Zeiss, Germany).

Biolayer Interferometry (BLI)

LNPs were initially prepared at a concentration of 200 μg/mL and subsequently diluted to 150 μg/mL, 100 μg/mL, 75 μg/mL, and 50 μg/mL, respectively. The number of LNP molecules (in moles) was calculated based on the specific formulation and the molar ratios of the individual lipid components. Biolayer interferometry (Octet RED96, Sartorius) was employed to analyze the binding affinity of different LNPs with DC 2.4. Amine-reactive second-generation (AR2G) biosensors (ForteBio) were incubated with Collagen type I solution (1 mg/mL) for 2 h at room temperature, followed by air-drying for 2 h. The collagen-coated biosensors were prewet for 10 min with 100 mL RPMI 1640, and immobilization of the DC 2.4 to the collagen-coated biosensors was then performed for 1 h at 30 °C. After capture of the cells, the biosensors were transferred to serum-starvation medium (RPMI 1640 containing 0.1% serum) and incubated overnight in a cell culture incubator. Afterward, the biosensors containing DC 2.4 were fixed with 4% formaldehyde in PBS for 15 min at room temperature. The time for each step was set as follows: 60 s for baseline phase, 120 s for LNP association phase, 90 s for LNP dissociation phase, and 220 s for regeneration phase. The kinetic curves (association and dissociation steps) were fitted to a 1:1 kinetics model to calculate K_D, the association rate constant (K_a), and the dissociation rate constant (K_d) by Data Analysis HT Software (Version 11.0.0.50, ForteBio).

Cellular Uptake Assay

To explore the endocytosis pathway of different LNPs, 5 × 10^5 of DC 2.4 were seeded in 12-well plates. Cells were pretreated with endocytic inhibitors for 1 h, including genistein (100 μM), chlorpromazine (30 μM), dynasore (15 μM), 5-(N-ethyl-N-isopropyl)amiloride (EIPA, 20 μM), LY294002 (50 μM), methyl-β-cyclodextrin (MBCD, 10 μM), and fucoidan (100 μg/mL). To investigate the temperature effect, DC 2.4 was incubated at 37 °C, 20 °C, and 4 °C for 1 h, respectively. Then the cells were washed with PBS and incubated with FITC-labeled LNPs for 1 h. Cells were collected for flow cytometry analysis by a CytoFLEX S flow cytometer (Beckman, CA, US) or stained with DAPI and observed by CLSM.

https://doi.org/10.1021/jacs.5c23209
J. Am. Chem. Soc. XXXX, XXX, XXX−XXX

Multiple Particle Tracking

Collagen hydrogels (1.5 mg/mL) were constructed as previously reported (31187973). In brief, collagen type I solution (2.4 mg/mL, 300 μL) was mixed with PBS (10×, 50 μL), sodium hydroxide (0.1 M, 10 μL), and complete RPMI medium (120 μL). Then the mixture was kept at 37 °C for 4 h to ensure the assembly of the intact collagen matrix. For the ex vivo tracking studies, 10 μL of LNPs was added onto 200 μL of collagen (I) hydrogels and incubated for 30 min before microscopy. The movement was captured for 20 s at an interval of 0.2 s. The trajectories for particles were analyzed using ImageJ (Version 1.54p). The time-averaged mean square displacement (MSD) and effective diffusivity (D_{eff}) were calculated using the following eqs 1 and 2, respectively:

$$\text{MSD}_t = (X_t - X_0)^2 + (Y_t - Y_0)^2 \tag{1}$$

$$D_{\text{eff}} = \frac{\text{MSD}}{4t} \tag{2}$$

Where x and y represent the coordinates of the particle, and t indicates the time scale.

Paracellular Transport Pathway of LNPs Across the Monolayer

The paracellular pathway was evaluated by detecting the integrity of tight junctions in the HUVEC monolayers. D-luciferin potassium (10 μg/mL) was added to the apical chamber of the monolayer and treated with PBS, A3-DM-LNPs, A3-DL-LNPs, ALC-0315-LNPs, and chitosan. The TEER was measured at 0, 1, 2, 4, 8, and 12 h, and 100 μL media from basolateral chambers were collected into the black 96-well plates, where another 100 μL of fresh media were added. The fluorescence intensity was determined by ID5Multi-Mode Microplate Readers (Molecular Devices) using excitation and emission wavelengths of 493 and 520 nm. The cumulative amount of D-luciferin potassium was calculated using a standard curve. Cells in the apical chamber treated with 0.5% chitosan (w/v) were used as the positive control.

Raman Spectra Imaging

All Raman spectra were acquired using a SuperVision Medicine Bio-SV Raman confocal microspectrometer, equipped with a green solid-state excitation laser (λ = 532 nm), a 63× water-immersion objective lens (Zeiss W Plan Apochromat, numerical aperture = 1.0), and a thermoelectrically cooled charge-coupled device (CCD) detector. The laser power was maintained at 20 mW for all measurements. Each spectrum was collected with an integration time of 0.8 s, yielding an xy-spatial resolution of 2.5 μm. Raman spectra were recorded over a wavenumber range of spanning 0−3600 cm^{-1}. The Raman imaging area was 500 × 500 μm for lymph node, liver, and spleen samples. In spontaneous Raman scattering, the intensity of a specific Raman band is directly proportional to the number of Raman scatterers. When experimental conditions are held constant, including optical configuration, excitation wavelength and power, acquisition time, and sample matrix, the Raman signals of lipid materials (A3-DS/DM/DL, A3-SS/SM-SL, A4-SS/SM/SL, and ALC-0315) exhibits a linear dependence on analyte concentration, which can be described as $I = ki \times C$, where ki represents a band-dependent proportionality constant encompassing instrumental and molecular factors. Raman intensities were quantified using ImageJ (Version 1.54p) and reported as arbitrary units (arb. units).[64,107]

In Vitro DC Activation and T Cell Expansion

Bone marrow cells were harvested by flushing the femurs and tibias of C57BL/6J mice and cultured in RPMI 1640 medium supplemented with 10% fetal bovine serum (FBS), 1% penicillin streptomycin , and 20 ng/mL granulocyte-macrophage colony-stimulating factor (GM-CSF). The medium was half-replaced every 2 days. Meanwhile, spleens were excised from C57BL/6J mice, and splenic lymphocytes were isolated using a commercial isolation kit according to the manufacturer's instructions. On day 8, nonadherent immature BMDCs were collected and seeded at a density of 1×10^6 cells per well in 12-well plates. After 24 h, BMDCs were treated with OVA mRNA (0.5 μg/mL) and siSTAT3 (25 nM) formulated in various LNP preparations, in complete medium at 37 °C in a 5% CO_2 incubator. After another 24 h, BMDCs were centrifuged and the supernatant was removed. Freshly isolated lymphocytes were added to the BMDCs for coculture, which was maintained for an additional 48 h. Following coculture, cells were harvested and stained with antibodies against CD11c, CD80, CD86, MHC II, and antimouse H-2Kb bound to SIINFEKL to assess DC activation and antigen presentation. Additional staining with PE-Cy7 anti-CD3, PerCP-Cy5.5 anti-CD8, APC anti-CD183, PE anti-CD62L, and PB450 anti-CD49b was performed to evaluate the proliferation and activation of $CD8^+$ T cells, NK cells, and Th1 cells. Cell proliferation was further analyzed using a BrdU (5-bromo-2′-deoxyuridine) cell proliferation kit, following the manufacturer's protocol. Flow cytometry was conducted using a CytoFLEX S flow cytometer (Beckman Coulter, CA, USA).

Transwell Coculture and Apoptosis Assay

BMDCs were cultured and treated as described above. Splenic lymphocytes were subsequently cocultured with these BMDCs in a transwell system for 48 h. For the apoptosis assay, the previously described splenic lymphocytes were seeded in the apical chamber of the transwell insert, while 5×10^6 C1498 cells were seeded in the basal chamber. After 24 h of coculture, C1498 cells were collected, washed with PBS, and centrifuged at 350 × g for 5 min. The splenocyte-conditioned medium was harvested for IFN-γ quantification using an ELISA assay. Apoptosis was assessed using a Dead Cell Apoptosis Kit with Annexin V-FITC and propidium iodide (PI), following the manufacturer's instructions. Stained cells were resuspended in 500 μL of staining buffer and analyzed by flow cytometry using a CytoFLEX S flow cytometer (Beckman Coulter, CA, USA).

Long-Term Immune Activation and Therapeutic Studies

All the 6- to 8-week-old female C57BL/6J mice and NOD-SCID/IL2λ-receptor null (NSG) mice that ranged from 20 to 22 g weight were purchased from Shanghai Sippe-Bk Lab Animal Co., Ltd. (Shanghai, China) and Shanghai Model Organisms Center, Inc. (Shanghai, China), respectively. All the animals were kept in the plastic cages according to "Principles of Animal Experiment Management" and "Guidelines for the Management and Use of Laboratory Animals". Mice were kept at 25 °C and a light/dark cycle (12/12 h) with unrestricted food and purified water availability. All animal experiments are carried out following the protocol approved by the Institutional Animal Care and Use Committee (IACUC) of China Pharmaceutical University (Protocol# 2022-05-050 and 2022-05-051).

For long-term immune activation, C57BL/6J mice were intravenously injected with A3-DM-LNPs, A3-DL-LNPs, and ALC-0315-LNPs (n = 3 per group). At 12 h, 1 d, 2 d, 3 d, 5 d, and 7 d postinjection, blood, spleen, and lymph node were collected. The long-term activation of $CD11c^+$ DCs, $CD3^+CD8^+$ T cells, $CD3^-CD56^+$ NK cells, and $CD3^+$ $CD4^+CD183^+$ Th1 cells in PBMCs, spleen, and lymph node was quantified by CytoFLEX S flow cytometer (Beckman, CA, US).

Human PBMCs were generously provided by Taicang First People's Hospital in accordance with protocol 2023-SR-014. Prior to the commencement of the study, written informed consent was obtained from all participants. The consent process ensured that participants were fully informed about the nature, purpose, and potential risks of the study. This consent was documented and is included in accordance with ethical research guidelines.

To establish the human PBMC model, 1×10^6 human PBMCs were intravenously injected into NSG mice to reconstitute the human immune system. Two weeks postengraftment, busulfan (20 mg/kg) was administered via intraperitoneal injection to each mouse. After 24 h, 5×10^5 of GFP-luciferase expressing HL-60 cells were injected intravenously to generate the PBMC-cell line-derived xenograft (PBMC-CDX) leukemia model. Two weeks after HL-60 implantation, mice were randomly assigned to receive one of the following treatments: PBS (G1), OVA mRNA-loaded LNPs (G2), or siSTAT3/OVA mRNA-loaded LNPs (G3), with A3-DL used as the RNA delivery vehicle. To evaluate the therapeutic efficacy of A3-DL-LNPs compared to the clinically approved ALC-0315-LNPs, we included ALC-0315-LNPs as a control in the same experimental setup. In these groups, both A3-DL-LNPs and ALC-0315-LNPs were loaded with siSTAT3/OVA mRNA and administered to the mice. Tumor progression was monitored using an IVIS Lumina Imaging System, and data were acquired and analyzed with Living Image software (Version 4.4, Caliper Life Sciences). At 4 weeks post-treatment, mice were euthanized, and samples of blood, spleen, lymph nodes, and bone marrow were collected for downstream analyses, including hematoxylin and eosin (H&E) staining, ELISA, and flow cytometry.

For the rotarod test, mice were placed on a rotating rod that accelerated from 4 to 40 rpm over 300 seconds. The latency to fall and corresponding speed were recorded to assess neuromuscular coordination. For flow cytometry, single-cell suspensions were stained with the following fluorophore-conjugated antibodies: APC anti-CD3, PE anti-CD4, PerCP-Cy5.5 anti-CD8, PE-Cy7 anti-CD183, eFluor450 anti-CD62L, APC-Cy7 anti-CD56, PerCP anti-CD11c, PE anti-CD80, APC anti-CD86, PE-Cy7 antimouse H-2Kb bound to SIINFEKL, eFluor450 anti-MHC-I, and eFluor780 anti-MHC-II. Data were acquired using a flow cytometer for immunophenotyping and antigen presentation analysis.

Evaluation of LNP Toxicity

Balb/C mice were intravenously administered with 12 different LNP formulations at total lipid of 3 mg/kg (low dose) and 6 mg/kg (high dose), respectively. After 24 h, blood was collected by retro-orbital bleeding, and serum was isolated. Liver toxicity markers, including ALT, AST, and ALP, as well as kidney markers creatinine and BUN, were quantified using commercial biochemical assay kits based on a colorimetric method, according to the manufacturer's instructions.

Statistical Analysis

The statistical analyses were performed using GraphPad Prism software (9.4.0). All data are displayed as means ± standard deviations (SD). Single comparisons were performed by student's *t*-test, and comparisons of multiple formulations were performed by one-way ANOVA. Significant differences between groups were indicated by $*P < 0.05$, $**P < 0.01$, $***P < 0.001$, and $****P < 0.0001$, respectively. $P < 0.05$ was considered statistically significant in all analyses.

■ ASSOCIATED CONTENT

Supporting Information

The Supporting Information is available free of charge at https://pubs.acs.org/doi/10.1021/jacs.5c23209.

> Experimental details; synthesis and characterization of imidazole-based ionizable lipids (^{1}H NMR); formulation screening and optimization workflow; LNP physicochemical characterization (size, PDI, pK_a, NMR, cryo-TEM, SAXS, AFM); cellular uptake and mechanism studies; BLI binding kinetics; diffusion/permeability assays; immunological assays; in vivo biodistribution, efficacy, and safety evaluation; supporting tables (PDF)

■ AUTHOR INFORMATION

Corresponding Authors

Lifang Yin − *Department of Pharmaceutics, China Pharmaceutical University, Nanjing 210009, China; NMPA Key Laboratory for Research and Evaluation of Pharmaceutical Preparations and Excipients, Key Laboratory of Drug Quality Control and Pharmacovigilance, and State Key Laboratory of Natural Medicine, China Pharmaceutical University, Nanjing 210009, China;* orcid.org/0000-0002-2825-3136; Phone: +86 (025)83271018; Email: lifangyin@cpu.edu.cn

Xiaofei Xin − *Department of Pharmaceutics, China Pharmaceutical University, Nanjing 210009, China; NMPA Key Laboratory for Research and Evaluation of Pharmaceutical Preparations and Excipients, China Pharmaceutical University, Nanjing 210009, China;* orcid.org/0000-0002-7618-0808; Phone: +86 (025) 83271018; Email: xxin@cpu.edu.cn

Na Li − *National Facility for Protein Science Shanghai, Shanghai Advanced Research Institute, Chinese Academy of Sciences, Shanghai 201210, China*; Phone: +86 (021) 20304861; Email: lina02@sari.ac.cn

Chao Qin − *Department of Pharmaceutics, China Pharmaceutical University, Nanjing 210009, China*; Phone: +86 (025)83271018; Email: nada77@163.com

Authors

Yifu Lyu − *Department of Pharmacy, Medical Supplies Center of Chinese PLA General Hospital, Beijing 100853, China*

Huanyu Qin − *Department of Pharmaceutics, China Pharmaceutical University, Nanjing 210009, China*

Jinyu Dai − *Department of Pharmaceutics, China Pharmaceutical University, Nanjing 210009, China*

Di Wu − *Department of Pharmaceutics, China Pharmaceutical University, Nanjing 210009, China*

Yu Ding − *Department of Pharmaceutics, China Pharmaceutical University, Nanjing 210009, China*

Qiang Tian − *State Key Laboratory of Environment-Friendly Energy Materials, School of Materials and Chemistry, Southwest University of Science and Technology, Mianyang 621010, China;* orcid.org/0000-0002-9811-4262

Complete contact information is available at: https://pubs.acs.org/10.1021/jacs.5c23209

Author Contributions

○X.X., Y.L., and H.Q. contributed equally to this work.

Notes

The authors declare no competing financial interest.

■ ACKNOWLEDGMENTS

The National Natural Science Foundation of China (82304410, 82473864), the Natural Science Foundation of Jiangsu Province (BK20221045), the National Center of Technology Innovation for Biopharmaceuticals (NCTIB2022HS01015), the Basic Research Program of Jiangsu (BK20253063), and "Double First-Class" initiative program in China Pharmaceutical University and the National Innovation and Entrepreneurship Training Program for Undergraduate are duly acknowledged for providing financial support for this work. We thank Xiaonan Ma of China Pharmaceutical University for providing technical assistance of LSM 800 confocal microscope on the Public Experimental Platform. We would like to thank the public platform of the State Key Laboratory of Natural Medicines for assistance in Biolayer Interferometry (BLI), and we grateful to Wei Jiang for her support of data acquisition and analysis. We thank Min-Hui Sun, Qin-Sheng Dai, and Jia Li for technical support from the Target Discovery Center of China Pharmaceutical University. We thank Zhe Song, Zhou Qiao, and Xi Chen in China Pharmaceutical University Center for Analysis and Testing for kind support on the manuscript. We thank the staff members of the Electron Microscopy System (https://cstr.cn/31129.02.NFPS.EMAS) at the National Facility for Protein Science in Shanghai (https://cstr.cn/31129.02.NFPS), for providing technical support and assistance in data collection and analysis. We thank the staff members of the beamline BL19U2 at the National Facility for Protein Science in Shanghai, for providing technical support and assistance in data collection and analysis. We extend our gratitude to Panqi Song for her assistance during the SAXS characterizations. We thank the staff members of the Molecular Imaging System at the National Facility for Protein Science in Shanghai (https://cstr.cn/31129.02.NFPS) for providing technical support and assistance in data collection and analysis. We acknowledge the Public Platform of Animal Experimental Center of China Pharmaceutical University for the using of living imaging system, and also thank Jie Zhao for her help with taking images.

■ REFERENCES

(1) Shimony, S.; Stahl, M.; Stone, R. M. Acute Myeloid Leukemia: 2025 Update on Diagnosis, Risk-Stratification, and Management. *Am. J. Hematol* **2025**, *100* (5), 860−891.

(2) Kewan, T.; Bahaj, W. S.; Gurnari, C.; Ogbue, O. D.; Mukherjee, S.; Advani, A.; Cook, J. R.; Rogers, H. J.; Carraway, H. E.; Balasubramanian, S. K.; Visconte, V.; Maciejewski, J. P. Clinical and molecular characteristics of extramedullary acute myeloid leukemias. *Leukemia* **2024**, *38* (9), 2032−2036.

(3) Solh, M.; Solomon, S.; Morris, L.; Holland, K.; Bashey, A. Extramedullary acute myelogenous leukemia. *Blood Rev* **2016**, *30* (5), 333−339.

(4) Perzolli, A.; Koedijk, J. B.; Zwaan, C. M.; Heidenreich, O. Targeting the innate immune system in pediatric and adult AML. *Leukemia* **2024**, *38* (6), 1191−1201.

(5) Du, S.; Yan, J.; Xue, Y.; Zhong, Y.; Dong, Y. Adoptive cell therapy for cancer treatment. *Exploration* **2023**, *3* (4), 20210058.

(6) Wang, F. Identification of tumor antigens and immune subtypes of acute myeloid leukemia for mRNA vaccine development. *Clin. Transl. Oncol* **2023**, *25* (7), 2204−2223.

(7) Sayour, E. J.; Boczkowski, D.; Mitchell, D. A.; Nair, S. K. Cancer mRNA vaccines: clinical advances and future opportunities. *Nat. Rev. Clin. Oncol* **2024**, *21* (7), 489−500.

(8) Anguille, S.; Van de Velde, A. L.; Smits, E. L.; Van Tendeloo, V. F.; Juliusson, G.; Cools, N.; Nijs, G.; Stein, B.; Lion, E.; Van Driessche, A.; Vandenbosch, I.; Verlinden, A.; Gadisseur, A. P.; Schroyens, W. A.; Muylle, L.; Vermeulen, K.; Maes, M. B.; Deiteren, K.; Malfait, R.; Gostick, E.; Lammens, M.; Couttenye, M. M.; Jorens, P.; Goossens, H.; Price, D. A.; Ladell, K.; Oka, Y.; Fujiki, F.; Oji, Y.; Sugiyama, H.; Berneman, Z. N. Dendritic cell vaccination as postremission treatment to prevent or delay relapse in acute myeloid leukemia. *Blood* **2017**, *130* (15), 1713−1721.

(9) Bandola-Simon, J.; Roche, P. A. Dysfunction of antigen processing and presentation by dendritic cells in cancer. *Mol. Immunol* **2019**, *113*, 31−37.

(10) Grootjans, J.; Kaser, A.; Kaufman, R. J.; Blumberg, R. S. The unfolded protein response in immunity and inflammation. *Nat. Rev. Immunol* **2016**, *16* (8), 469−484.

(11) Alshamsan, A.; Haddadi, A.; Hamdy, S.; Samuel, J.; El-Kadi, A. O.; Uludağ, H.; Lavasanifar, A. STAT3 silencing in dendritic cells by siRNA polyplexes encapsulated in PLGA nanoparticles for the modulation of anticancer immune response. *Mol. Pharmaceutics* **2010**, *7* (5), 1643−1654.

(12) Gao, Y.; Ding, Y.; Tai, X. R.; Zhang, C.; Wang, D. Ponatinib: An update on its drug targets, therapeutic potential and safety. *Biochim. Biophys. Acta, Rev. Cancer* **2023**, *1878* (5), 188949.

(13) Tan, F. H.; Putoczki, T. L.; Lou, J.; Hinde, E.; Hollande, F.; Giraud, J.; Stylli, S. S.; Paradiso, L.; Zhu, H. J.; Sieber, O. M.; Luwor, R. B. Ponatinib Inhibits Multiple Signaling Pathways Involved in STAT3 Signaling and Attenuates Colorectal Tumor Growth. *Cancers* **2018**, *10* (12), 526.

(14) Bieerkehazhi, S.; Chen, Z.; Zhao, Y.; Yu, Y.; Zhang, H.; Vasudevan, S. A.; Woodfield, S. E.; Tao, L.; Yi, J. S.; Muscal, J. A.; Pang, J. C.; Guan, S.; Zhang, H.; Nuchtern, J. G.; Li, H.; Li, H.; Yang, J. Novel Src/Abl tyrosine kinase inhibitor bosutinib suppresses neuroblastoma growth via inhibiting Src/Abl signaling. *Oncotarget* **2017**, *8* (1), 1469−1480.

(15) Steinbach, A.; Clark, S. M.; Clemmons, A. B. Bosutinib: a novel src/abl kinase inhibitor for chronic myelogenous leukemia. *J. Adv. Pract Oncol* **2013**, *4* (6), 451−455.

(16) Rezvani, K.; Barrett, J. STAT3: the "Achilles" heel for AML? *Blood* **2014**, *123* (1), 1−2.

(17) Kortylewski, M.; Kujawski, M.; Wang, T.; Wei, S.; Zhang, S.; Pilon-Thomas, S.; Niu, G.; Kay, H.; Mulé, J.; Kerr, W. G.; Jove, R.; Pardoll, D.; Yu, H. Inhibiting Stat3 signaling in the hematopoietic system elicits multicomponent antitumor immunity. *Nat. Med* **2005**, *11* (12), 1314−1321.

(18) Ferrajoli, A.; Faderl, S.; Van, Q.; Harris, D. M.; Priebe, W.; Kantarjian, H. M.; Talpaz, M.; Estrov, Z. WP-1066, a Next-Generation Member of JAK-Stat Inhibitors, Induces Cell Cycle Arrest, Abrogates Proliferation, and Induces Apoptosis of Acute Myeloid Leukemia (AML) Cells. *Blood* **2004**, *104* (11), 1169−1169.

(19) Miao, Y.; Fu, C.; Yu, Z.; Yu, L.; Tang, Y.; Wei, M. Current status and trends in small nucleic acid drug development: Leading the future. *Acta Pharm. Sin B* **2024**, *14* (9), 3802−3817.

(20) Zai, W.; Yang, M.; Jiang, K.; Guan, J.; Wang, H.; Hu, K.; Huang, C.; Chen, J.; Fu, W.; Zhan, C.; Yuan, Z. Optimized RNA interference therapeutics combined with interleukin-2 mRNA for treating hepatitis B virus infection. *Signal Transduct Target Ther* **2024**, *9* (1), 150.

(21) Hamilton, A. G.; Swingle, K. L.; Joseph, R. A.; Mai, D.; Gong, N.; Billingsley, M. M.; Alameh, M. G.; Weissman, D.; Sheppard, N. C.; June, C. H.; Mitchell, M. J. Ionizable Lipid Nanoparticles with Integrated Immune Checkpoint Inhibition for mRNA CAR T Cell Engineering. *Adv. Healthcare Mater* **2023**, *12* (30), No. e2301515.

(22) Ball, R. L.; Hajj, K. A.; Vizelman, J.; Bajaj, P.; Whitehead, K. A. Lipid Nanoparticle Formulations for Enhanced Co-delivery of siRNA and mRNA. *Nano Lett* **2018**, *18* (6), 3814−3822.

(23) Kloczewiak, M.; Banks, J. M.; Jin, L.; Brader, M. L. A Biopharmaceutical Perspective on Higher-Order Structure and Thermal Stability of mRNA Vaccines. *Mol. Pharmaceutics* **2022**, *19* (7), 2022−2031.

(24) Kulkarni, J. A.; Darjuan, M. M.; Mercer, J. E.; Chen, S.; van der Meel, R.; Thewalt, J. L.; Tam, Y. Y. C.; Cullis, P. R. On the Formation and Morphology of Lipid Nanoparticles Containing Ionizable Cationic Lipids and siRNA. *ACS Nano* **2018**, *12* (5), 4787−4795.

(25) Zhang, C.; Tian, F. J.; Zuo, H. W.; Qiu, Q. Y.; Zhang, J. H.; Wei, W.; Tan, Z. J.; Zhang, Y.; Wu, W. Q.; Dai, L.; Zhang, X. H. Counterintuitive DNA destabilization by monovalent salt at high concentrations due to overcharging. *Nat. Commun* **2025**, *16* (1), 113.

(26) Lipfert, J.; Doniach, S.; Das, R.; Herschlag, D. Understanding nucleic acid-ion interactions. *Annu. Rev. Biochem* **2014**, *83*, 813−841.

(27) Bai, Y.; Das, R.; Millett, I. S.; Herschlag, D.; Doniach, S. Probing counterion modulated repulsion and attraction between nucleic acid duplexes in solution. *Proc. Natl. Acad. Sci. U. S. A* **2005**, *102* (4), 1035−1040.

(28) Zhou, F.; Huang, L.; Li, S.; Yang, W.; Chen, F.; Cai, Z.; Liu, X.; Xu, W.; Lehto, V.-P.; Lächelt, U.; et al. From structural design to delivery: mRNA therapeutics for cancer immunotherapy. *Exploration* **2024**, *4* (2), 20210146.

(29) Pilkington, C. P.; Gispert, I.; Chui, S. Y.; Seddon, J. M.; Elani, Y. Engineering a nanoscale liposome-in-liposome for in situ biochemical synthesis and multi-stage release. *Nat. Chem* **2024**, *16* (10), 1612−1620.

(30) Yu, H.; Iscaro, J.; Dyett, B.; Zhang, Y.; Seibt, S.; Martinez, N.; White, J.; Drummond, C. J.; Bozinovski, S.; Zhai, J. Inverse Cubic and Hexagonal Mesophase Evolution within Ionizable Lipid Nanoparticles

Correlates with mRNA Transfection in Macrophages. *J. Am. Chem. Soc* **2023**, *145*, 24765−24774.

(31) Fan, B.; Wan, J.; Zhai, J.; Chen, X.; Thang, S. H. Triggered Degradable Colloidal Particles with Ordered Inverse Bicontinuous Cubic and Hexagonal Mesophases. *ACS Nano* **2021**, *15* (3), 4688−4698.

(32) Meshanni, J. A.; Stevenson, E. R.; Zhang, D.; Sun, R.; Ona, N. A.; Reagan, E. K.; Abramova, E.; Guo, C. J.; Wilkinson, M.; Baboo, I.; Yang, Y.; Pan, L.; Maurya, D. S.; Percec, V.; Li, Y.; Gow, A.; Weissman, D.; Atochina-Vasserman, E. N. Targeted delivery of TGF-β mRNA to murine lung parenchyma using one-component ionizable amphiphilic Janus Dendrimers. *Nat. Commun* **2025**, *16* (1), 1806.

(33) Pattipeiluhu, R.; Zeng, Y.; Hendrix, M.; Voets, I. K.; Kros, A.; Sharp, T. H. Liquid crystalline inverted lipid phases encapsulating siRNA enhance lipid nanoparticle mediated transfection. *Nat. Commun* **2024**, *15* (1), 1303.

(34) Salvador-Castell, M.; Brooks, N. J.; Peters, J.; Oger, P. Induction of non-lamellar phases in archaeal lipids at high temperature and high hydrostatic pressure by apolar polyisoprenoids. *Biochim. Biophys. Acta, Biomembr* **2020**, *1862* (2), 183130.

(35) Percec, V.; Wilson, D. A.; Leowanawat, P.; Wilson, C. J.; Hughes, A. D.; Kaucher, M. S.; Hammer, D. A.; Levine, D. H.; Kim, A. J.; Bates, F. S.; Davis, K. P.; Lodge, T. P.; Klein, M. L.; DeVane, R. H.; Aqad, E.; Rosen, B. M.; Argintaru, A. O.; Sienkowska, M. J.; Rissanen, K.; Nummelin, S.; Ropponen, J. Self-assembly of Janus dendrimers into uniform dendrimersomes and other complex architectures. *Science* **2010**, *328* (5981), 1009−1014.

(36) Doktorova, M.; Symons, J. L.; Levental, I. Structural and functional consequences of reversible lipid asymmetry in living membranes. *Nat. Chem. Biol* **2020**, *16* (12), 1321−1330.

(37) Lee, T. H.; Charchar, P.; Separovic, F.; Reid, G. E.; Yarovsky, I.; Aguilar, M. I. The intricate link between membrane lipid structure and composition and membrane structural properties in bacterial membranes. *Chem. Sci* **2024**, *15* (10), 3408−3427.

(38) Liu, Y.; He, F.; Chen, L.; Zhang, Y.; Zhang, H.; Xiao, J.; Meng, Q. Imidazolyl Lipids Enhanced LNP Endosomal Escape for Ferroptosis RNAi Treatment of Cancer. *Small* **2024**, *20* (40), No. e2402362.

(39) Dong, W.; Li, Z.; Hou, T.; Shen, Y.; Guo, Z.; Su, Y. T.; Chen, Z.; Pan, H.; Jiang, W.; Wang, Y. Multicomponent Synthesis of Imidazole-Based Ionizable Lipids for Highly Efficient and Spleen-Selective Messenger RNA Delivery. *J. Am. Chem. Soc* **2024**, *146* (22), 15085−15095.

(40) Paulisch, T. O.; Bornemann, S.; Herzog, M.; Kudruk, S.; Roling, L.; Linard Matos, A. L.; Galla, H. J.; Gerke, V.; Winter, R.; Glorius, F. An Imidazolium-Based Lipid Analogue as a Gene Transfer Agent. *Chemistry* **2020**, *26* (71), 17176−17182.

(41) Miao, L.; Li, L.; Huang, Y.; Delcassian, D.; Chahal, J.; Han, J.; Shi, Y.; Sadtler, K.; Gao, W.; Lin, J.; Doloff, J. C.; Langer, R.; Anderson, D. G. Delivery of mRNA vaccines with heterocyclic lipids increases anti-tumor efficacy by STING-mediated immune cell activation. *Nat. Biotechnol* **2019**, *37* (10), 1174−1185.

(42) Dong, Y.; Ma, T.; Xu, T.; Feng, Z.; Li, Y.; Song, L.; Yao, X.; Ashby, C. R., Jr.; Hao, G. F. Characteristic roadmap of linker governs the rational design of PROTACs. *Acta Pharm. Sin B* **2024**, *14* (10), 4266−4295.

(43) Ni, H.; Hatit, M. Z. C.; Zhao, K.; Loughrey, D.; Lokugamage, M. P.; Peck, H. E.; Cid, A. D.; Muralidharan, A.; Kim, Y.; Santangelo, P. J.; Dahlman, J. E. Piperazine-derived lipid nanoparticles deliver mRNA to immune cells in vivo. *Nat. Commun* **2022**, *13* (1), 4766.

(44) Carrasco, M. J.; Alishetty, S.; Alameh, M. G.; Said, H.; Wright, L.; Paige, M.; Soliman, O.; Weissman, D.; Cleveland, T. E. T.; Grishaev, A.; Buschmann, M. D. Ionization and structural properties of mRNA lipid nanoparticles influence expression in intramuscular and intravascular administration. *Commun. Biol* **2021**, *4* (1), 956.

(45) Patel, P.; Ibrahim, N. M.; Cheng, K. The Importance of Apparent pKa in the Development of Nanoparticles Encapsulating siRNA and mRNA. *Trends Pharmacol. Sci* **2021**, *42* (6), 448−460.

(46) Jayaraman, M.; Ansell, S. M.; Mui, B. L.; Tam, Y. K.; Chen, J.; Du, X.; Butler, D.; Eltepu, L.; Matsuda, S.; Narayanannair, J. K.; Rajeev, K. G.; Hafez, I. M.; Akinc, A.; Maier, M. A.; Tracy, M. A.; Cullis, P. R.; Madden, T. D.; Manoharan, M.; Hope, M. J. Maximizing the potency of siRNA lipid nanoparticles for hepatic gene silencing in vivo. *Angew. Chem., Int. Ed. Engl* **2012**, *51* (34), 8529−8533.

(47) Dilliard, S. A.; Cheng, Q.; Siegwart, D. J. On the mechanism of tissue-specific mRNA delivery by selective organ targeting nanoparticles. *Proc. Natl. Acad. Sci. U. S. A* **2021**, *118* (52), No. e2109256118.

(48) Li, M.; Schroder, R.; Ozuguzel, U.; Corts, T. M.; Liu, Y.; Zhao, Y.; Xu, W.; Ling, J.; Templeton, A. C.; Chaudhuri, B.; Gindy, M.; Wagner, A.; Su, Y. Molecular Insight into Lipid Nanoparticle Assembly from NMR Spectroscopy and Molecular Dynamics Simulation. *Mol. Pharmaceutics* **2025**, *22* (4), 2193−2212.

(49) Ueda, K.; Sakagawa, Y.; Saito, T.; Fujimoto, T.; Nakamura, M.; Sakuma, F.; Kaneko, S.; Tokumoto, T.; Nishimura, K.; Takeda, J.; Arai, Y.; Yamamoto, K.; Ikeda, Y.; Higashi, K.; Moribe, K. Molecular-Level Structural Analysis of siRNA-Loaded Lipid Nanoparticles by (1)H NMR Relaxometry: Impact of Lipid Composition on Their Structural Properties. *Mol. Pharmaceutics* **2023**, *20* (9), 4729−4742.

(50) Donida, B.; Tauffner, B.; Raabe, M.; Immich, M. F.; de Farias, M. A.; de Sá Coutinho, D.; Machado, A. Z.; Kessler, R. G.; Portugal, R. V.; Bernardi, A.; Frozza, R.; Moura, D. J.; Poletto, F.; Vargas, C. R. Monoolein-based nanoparticles for drug delivery to the central nervous system: A platform for lysosomal storage disorder treatment. *Eur. J. Pharm. Biopharm* **2018**, *133*, 96−103.

(51) Chen, X.; Zhong, S.; Hou, Y.; Cao, R.; Wang, W.; Li, D.; Dai, Q.; Kim, D.; Xi, P. Superresolution structured illumination microscopy reconstruction algorithms: a review. *Light Sci. Appl* **2023**, *12* (1), 172.

(52) Yazdi, M.; Pöhmerer, J.; Hasanzadeh Kafshgari, M.; Seidl, J.; Grau, M.; Höhn, M.; Vetter, V.; Hoch, C. C.; Wollenberg, B.; Multhoff, G.; Bashiri Dezfouli, A.; Wagner, E. In Vivo Endothelial Cell Gene Silencing by siRNA-LNPs Tuned with Lipoamino Bundle Chemical and Ligand Targeting. *Small* **2024**, *20* (42), No. e2400643.

(53) Bogaert, B.; Debisschop, A.; Ehouarne, T.; Van Eeckhoutte, H. P.; De Volder, J.; Jacobs, A.; Pottie, E.; De Rycke, R.; Crabbé, A.; Mestdagh, P.; Lentacker, I.; Brusselle, G. G.; Stove, C.; Verstraelen, S.; Maes, T.; Bracke, K. R.; De Smedt, S. C.; Raemdonck, K. Selective Replacement of Cholesterol with Cationic Amphiphilic Drugs Enables the Design of Lipid Nanoparticles with Improved RNA Delivery. *Nano Lett* **2024**, *24* (10), 2961−2971.

(54) Et-Thakafy, O.; Delorme, N.; Gaillard, C.; Mériadec, C.; Artzner, F.; Lopez, C.; Guyomarc'h, F. Mechanical Properties of Membranes Composed of Gel-Phase or Fluid-Phase Phospholipids Probed on Liposomes by Atomic Force Spectroscopy. *Langmuir* **2017**, *33* (21), 5117−5126.

(55) Song, Y.; Wu, Y.; Xu, L.; Jiang, T.; Tang, C.; Yin, C. Caveolae-Mediated Endocytosis Drives Robust siRNA Delivery of Polymeric Nanoparticles to Macrophages. *ACS Nano* **2021**, *15* (5), 8267−8282.

(56) Angelova, M. I.; Bitbol, A. F.; Seigneuret, M.; Staneva, G.; Kodama, A.; Sakuma, Y.; Kawakatsu, T.; Imai, M.; Puff, N. pH sensing by lipids in membranes: The fundamentals of pH-driven migration, polarization and deformations of lipid bilayer assemblies. *Biochim. Biophys. Acta, Biomembr* **2018**, *1860* (10), 2042−2063.

(57) Gilleron, J.; Querbes, W.; Zeigerer, A.; Borodovsky, A.; Marsico, G.; Schubert, U.; Manygoats, K.; Seifert, S.; Andree, C.; Stöter, M.; Epstein-Barash, H.; Zhang, L.; Koteliansky, V.; Fitzgerald, K.; Fava, E.; Bickle, M.; Kalaidzidis, Y.; Akinc, A.; Maier, M.; Zerial, M. Image-based analysis of lipid nanoparticle-mediated siRNA delivery, intracellular trafficking and endosomal escape. *Nat. Biotechnol* **2013**, *31* (7), 638−646.

(58) Sahay, G.; Querbes, W.; Alabi, C.; Eltoukhy, A.; Sarkar, S.; Zurenko, C.; Karagiannis, E.; Love, K.; Chen, D.; Zoncu, R.; Buganim, Y.; Schroeder, A.; Langer, R.; Anderson, D. G. Efficiency of siRNA delivery by lipid nanoparticles is limited by endocytic recycling. *Nat. Biotechnol* **2013**, *31* (7), 653−658.

(59) Li, Q.; Wen, C.; Yang, J.; Zhou, X.; Zhu, Y.; Zheng, J.; Cheng, G.; Bai, J.; Xu, T.; Ji, J.; Jiang, S.; Zhang, L.; Zhang, P. Zwitterionic Biomaterials. *Chem. Rev* **2022**, *122* (23), 17073−17154.

(60) Lettieri, A.; Oleari, R.; van den Munkhof, M. H.; van Battum, E. Y.; Verhagen, M. G.; Tacconi, C.; Spreafico, M.; Paganoni, A. J. J.; Azzarelli, R.; Andre, V.; et al. SEMA6A drives GnRH neuron-dependent puberty onset by tuning median eminence vascular permeability. *Nat. Commun* **2023**, *14* (1), 8097.

(61) Deng, F.; Kim, K. S.; Moon, J.; Bae, Y. H. Bile Acid Conjugation on Solid Nanoparticles Enhances ASBT-Mediated Endocytosis and Chylomicron Pathway but Weakens the Transcytosis by Inducing Transport Flow in a Cellular Negative Feedback Loop. *Adv. Sci* **2022**, *9* (21), No. e2201414.

(62) Yu, X.; Dai, Y.; Zhao, Y.; Qi, S.; Liu, L.; Lu, L.; Luo, Q.; Zhang, Z. Melittin-lipid nanoparticles target to lymph nodes and elicit a systemic anti-tumor immune response. *Nat. Commun* **2020**, *11* (1), 1110.

(63) Hamilton, A. G.; Swingle, K. L.; Thatte, A. S.; Mukalel, A. J.; Safford, H. C.; Billingsley, M. M.; El-Mayta, R. D.; Han, X.; Nachod, B. E.; Joseph, R. A.; Metzloff, A. E.; Mitchell, M. J. High-Throughput In Vivo Screening Identifies Differential Influences on mRNA Lipid Nanoparticle Immune Cell Delivery by Administration Route. *ACS Nano* **2024**, *18* (25), 16151−16165.

(64) LaLone, V.; Aizenshtadt, A.; Goertz, J.; Skottvoll, F. S.; Mota, M. B.; You, J.; Zhao, X.; Berg, H. E.; Stokowiec, J.; Yu, M.; Schwendeman, A.; Scholz, H.; Wilson, S. R.; Krauss, S.; Stevens, M. M. Quantitative chemometric phenotyping of three-dimensional liver organoids by Raman spectral imaging. *Cell Rep. Methods* **2023**, 3 (4), 100440.

(65) Gao, X.; Lang, X.; El Khoury, E.; Wei, M.; Qian, N.; Min, W. Quantitative Label-Free Chemical Imaging of PLGA Nanoparticles in Cells and Tissues with Single-Particle Sensitivity. *Nano Lett* **2024**, *24* (3), 1024−1033.

(66) Wang, W.; Deng, S.; Lin, J.; Ouyang, D. Modeling on in vivo disposition and cellular transportation of RNA lipid nanoparticles via quantum mechanics/physiologically-based pharmacokinetic approaches. *Acta Pharm. Sin B* **2024**, *14* (10), 4591−4607.

(67) Huang, Z.; Sun, K.; Luo, Z.; Zhang, J.; Zhou, H.; Yin, H.; Liang, Z.; You, J. Spleen-targeted delivery systems and strategies for spleen-related diseases. *J. Controlled Release* **2024**, *370*, 773−797.

(68) Alexandre, Y. O.; Mueller, S. N. Splenic stromal niches in homeostasis and immunity. *Nat. Rev. Immunol* **2023**, *23* (11), 705−719.

(69) Mebius, R. E.; Kraal, G. Structure and function of the spleen. *Nat. Rev. Immunol* **2005**, *5* (8), 606−616.

(70) Ugur, M.; Labios, R. J.; Fenton, C.; Knöpper, K.; Jobin, K.; Imdahl, F.; Golda, G.; Hoh, K.; Grafen, A.; Kaisho, T.; et al. Lymph node medulla regulates the spatiotemporal unfolding of resident dendritic cell networks. *Immunity* **2023**, *56* (8), 1778−1793.e10.

(71) Fang, V.; Chaluvadi, V. S.; Ramos-Perez, W. D.; Mendoza, A.; Baeyens, A.; Rivera, R.; Chun, J.; Cammer, M.; Schwab, S. R. Gradients of the signaling lipid S1P in lymph nodes position natural killer cells and regulate their interferon-γ response. *Nat. Immunol* **2017**, *18* (1), 15−25.

(72) Muraoka, D.; Harada, N.; Hayashi, T.; Tahara, Y.; Momose, F.; Sawada, S.; Mukai, S. A.; Akiyoshi, K.; Shiku, H. Nanogel-based immunologically stealth vaccine targets macrophages in the medulla of lymph node and induces potent antitumor immunity. *ACS Nano* **2014**, *8* (9), 9209−9218.

(73) Hosseini-Kharat, M.; Bremmell, K. E.; Prestidge, C. A. Why do lipid nanoparticles target the liver? Understanding of biodistribution and liver-specific tropism. *Mol. Ther Methods Clin Dev* **2025**, *33* (1), 101436.

(74) Kim, M.; Jeong, M.; Hur, S.; Cho, Y.; Park, J.; Jung, H.; Seo, Y.; Woo, H. A.; Nam, K. T.; Lee, K.; et al. Engineered ionizable lipid nanoparticles for targeted delivery of RNA therapeutics into different types of cells in the liver. *Sci. Adv* **2021**, 7 (9), No. eabf4398.

(75) Zhao, Y.; Zhao, S.; Liu, S.; Ye, W.; Chen, W. D. Kupffer cells, the limelight in the liver regeneration. *Int. Immunopharmacol* **2025**, *146*, 113808.

(76) Bonnardel, J.; T'Jonck, W.; Gaublomme, D.; Browaeys, R.; Scott, C. L.; Martens, L.; Vanneste, B.; De Prijck, S.; Nedospasov, S. A.; Kremer, A.; et al. Stellate Cells, Hepatocytes, and Endothelial Cells Imprint the Kupffer Cell Identity on Monocytes Colonizing the Liver Macrophage Niche. *Immunity* **2019**, *51* (4), 638−654.e9.

(77) Li, B.; Raji, I. O.; Gordon, A. G. R.; Sun, L.; Raimondo, T. M.; Oladimeji, F. A.; Jiang, A. Y.; Varley, A.; Langer, R. S.; Anderson, D. G. Accelerating ionizable lipid discovery for mRNA delivery using machine learning and combinatorial chemistry. *Nat. Mater* **2024**, *23* (7), 1002−1008.

(78) Hassett, K. J.; Rajlic, I. L.; Bahl, K.; White, R.; Cowens, K.; Jacquinet, E.; Burke, K. E. mRNA vaccine trafficking and resulting protein expression after intramuscular administration. *Mol. Ther Nucleic Acids* **2024**, *35* (1), 102083.

(79) Lewis, S. M.; Williams, A.; Eisenbarth, S. C. Structure and function of the immune system in the spleen. *Sci. Immunol* **2019**, *4* (33), No. eaau6085.

(80) Morgan, D. M.; Horton, B. L.; Bhandarkar, V.; Van, R.; Dinter, T.; Zagorulya, M.; Love, J. C.; Spranger, S. Expansion of tumor-reactive CD8(+) T cell clonotypes occurs in the spleen in response to immune checkpoint blockade. *Sci. Immunol* **2024**, *9* (99), No. eadi3487.

(81) Salvagno, C.; Mandula, J. K.; Rodriguez, P. C.; Cubillos-Ruiz, J. R. Decoding endoplasmic reticulum stress signals in cancer cells and antitumor immunity. *Trends Cancer* **2022**, *8* (11), 930−943.

(82) Philippe, C.; Jaud, M.; Féral, K.; Gay, A.; Van Den Berghe, L.; Farce, M.; Bousquet, M.; Pyronnet, S.; Mazzolini, L.; Rouault-Pierre, K.; Touriol, C. Pivotal role of the endoplasmic reticulum stress-related XBP1s/miR-22/SIRT1 axis in acute myeloid leukemia apoptosis and response to chemotherapy. *Leukemia* **2024**, *38* (8), 1764−1776.

(83) Pan, Q.; Xin, X.; Mahto, S.; Dong, Y.; Kumar, V.; Hyde, R. K.; Gupta, N.; Bhatt, V. R.; Mahato, R. I. Anti-CLL1 liposome loaded with miR-497−5p and venetoclax as a novel therapeutic strategy in acute myeloid leukemia. *Mol. Ther* **2024**, *32* (11), 4058−4074.

(84) Lasry, A.; Nadorp, B.; Fornerod, M.; Nicolet, D.; Wu, H.; Walker, C. J.; Sun, Z.; Witkowski, M. T.; Tikhonova, A. N.; Guillamot-Ruano, M.; Cayanan, G.; Yeaton, A.; Robbins, G.; Obeng, E. A.; Tsirigos, A.; Stone, R. M.; Byrd, J. C.; Pounds, S.; Carroll, W. L.; Gruber, T. A.; Eisfeld, A. K.; Aifantis, I. An inflammatory state remodels the immune microenvironment and improves risk stratification in acute myeloid leukemia. *Nat. Cancer* **2022**, *4* (1), 27−42.

(85) Zhang, W.; Shi, Y.; Oyang, L.; Cui, S.; Li, S.; Li, J.; Liu, L.; Li, Y.; Peng, M.; Tan, S.; Xia, L.; Lin, J.; Xu, X.; Wu, N.; Peng, Q.; Tang, Y.; Luo, X.; Liao, Q.; Jiang, X.; Zhou, Y. Endoplasmic reticulum stress-a key guardian in cancer. *Cell Death Discovery* **2024**, *10* (1), 343.

(86) Manoury, B.; Maisonneuve, L.; Podsypanina, K. The role of endoplasmic reticulum stress in the MHC class I antigen presentation pathway of dendritic cells. *Mol. Immunol* **2022**, *144*, 44−48.

(87) Kim, K.; Lee, S.; Yoon, J.; Heo, J.; Choi, C.; Park, Y. Three-dimensional label-free imaging and quantification of lipid droplets in live hepatocytes. *Sci. Rep* **2016**, *6*, 36815.

(88) Xu, H.; Li, Y.; Gao, Y. The role of immune cells settled in the bone marrow on adult hematopoietic stem cells. *Cell. Mol. Life Sci* **2024**, *81* (1), 420.

(89) Cruz de Casas, P.; Knöpper, K.; Dey Sarkar, R.; Kastenmüller, W. Same yet different - how lymph node heterogeneity affects immune responses. *Nat. Rev. Immunol* **2024**, *24* (5), 358−374.

(90) Nguyen, N. T.; Youn, Y. S. Strategies to Design and Optimize Artificial Antigen-Presenting Cells for T Cell Expansion in Cancer Immunotherapy. *Adv. Funct. Mater* **2025**, *35* (41), 2426047.

(91) Huang, H.; Hao, S.; Li, F.; Ye, Z.; Yang, J.; Xiang, J. CD4+ Th1 cells promote CD8+ Tc1 cell survival, memory response, tumor localization and therapy by targeted delivery of interleukin 2 via acquired pMHC I complexes. *Immunology* **2007**, *120* (2), 148−159.

(92) Sauter, C.; Morin, T.; Guidez, F.; Simonet, J.; Fournier, C.; Row, C.; Masnikov, D.; Pernon, B.; Largeot, A.; Aznague, A.; Hérault, Y.; Sauvageau, G.; Maynadié, M.; Callanan, M.; Bastie, J. N.; Aucagne, R.; Delva, L. Protein arginine methyltransferase 2 controls inflammatory signaling in acute myeloid leukemia. *Commun. Biol* **2024**, 7 (1), 753.

(93) Nurieva, R. I.; Chung, Y. Understanding the development and function of T follicular helper cells. *Cell. Mol. Immunol* **2010**, *7* (3), 190−197.

(94) Laumont, C. M.; Nelson, B. H. IgA transcytosis: A new weapon in the immune response to cancer? *Cancer Cell* **2021**, *39* (5), 607−609.

(95) Bolouri, H.; Ries, R. E.; Wiedeman, A. E.; Hylkema, T.; Scheiding, S.; Gersuk, V. H.; O'Brien, K.; Nguyen, Q. A.; Smith, J. L.; Alice Long, S.; Meshinchi, S. Inflammatory bone marrow signaling in pediatric acute myeloid leukemia distinguishes patients with poor outcomes. *Nat. Commun* **2022**, *13* (1), 7186.

(96) Lee, C. C.; Hsu, S. C.; Lai, L. L.; Lu, K. L. Chair-boat form transformation of piperazine-containing ligand toward the preparation of dirhenium metallacycles. *Inorg. Chem* **2009**, *48* (14), 6329−6331.

(97) Ye, Z.; Yang, W.; Wang, C.; Zheng, Y.; Chi, W.; Liu, X.; Huang, Z.; Li, X.; Xiao, Y. Quaternary Piperazine-Substituted Rhodamines with Enhanced Brightness for Super-Resolution Imaging. *J. Am. Chem. Soc* **2019**, *141* (37), 14491−14495.

(98) Zhi, Q.; Liu, W.; Jiang, R.; Zhan, X.; Jin, Y.; Chen, X.; Yang, X.; Wang, K.; Cao, W.; Qi, D.; Jiang, J. Piperazine-Linked Metal-phthalocyanine Frameworks for Highly Efficient Visible-Light-Driven H(2)O(2) Photosynthesis. *J. Am. Chem. Soc* **2022**, *144* (46), 21328−21336.

(99) Pota, K.; Johnston, H. M.; Madarasi, E.; Tircsó, G.; Green, K. N. Synthesis and characterization of two piperazine containing macrocycles and their transition metal complexes. *J. Inorg. Biochem* **2023**, *241*, 112124.

(100) Wang, D.; Huang, X.-F.; Hong, B.; Song, X. T.; Hu, L.; Jiang, M.; Zhang, B.; Ning, H.; Li, Y.; Xu, C.; et al. Efficacy of intracellular immune checkpoint-silenced DC vaccine. *JCI Insight* **2018**, *3* (3), No. e98368.

(101) Li, K.; Du, Y.; Cai, Y.; Liu, W.; Lv, Y.; Huang, B.; Zhang, L.; Wang, Z.; Liu, P.; Sun, Q.; Li, N.; Zhu, M.; Bosco, B.; Li, L.; Wu, W.; Wu, L.; Li, J.; Wang, Q.; Hong, M.; Qian, S. Single-cell analysis reveals the chemotherapy-induced cellular reprogramming and novel therapeutic targets in relapsed/refractory acute myeloid leukemia. *Leukemia* **2023**, *37* (2), 308−325.

(102) Lamba, J. K.; Chauhan, L.; Shin, M.; Loken, M. R.; Pollard, J. A.; Wang, Y. C.; Ries, R. E.; Aplenc, R.; Hirsch, B. A.; Raimondi, S. C.; Walter, R. B.; Bernstein, I. D.; Gamis, A. S.; Alonzo, T. A.; Meshinchi, S. CD33 Splicing Polymorphism Determines Gemtuzumab Ozogamicin Response in De Novo Acute Myeloid Leukemia: Report From Randomized Phase III Children's Oncology Group Trial AAML0531. *J. Clin. Oncol* **2017**, *35* (23), 2674−2682.

(103) Brady, M. T.; Miller, A.; Sait, S. N.; Ford, L. A.; Minderman, H.; Wang, E. S.; Lee, K. P.; Baumann, H.; Wetzler, M. Down-regulation of signal transducer and activator of transcription 3 improves human acute myeloid leukemia-derived dendritic cell function. *Leuk. Res* **2013**, *37* (7), 822−828.

(104) Dömling, A. Recent developments in isocyanide based multicomponent reactions in applied chemistry. *Chem. Rev* **2006**, *106* (1), 17−89.

(105) Wan, J. P.; Gan, L.; Liu, Y. Transition metal-catalyzed C-H bond functionalization in multicomponent reactions: a tool toward molecular diversity. *Org. Biomol Chem* **2017**, *15* (43), 9031−9043.

(106) Kohlbrecher, J.; Breßler, I. Updates in SASfit for fitting analytical expressions and numerical models to small-angle scattering patterns. *J. Appl. Crystallogr* **2022**, *55* (6), 1677−1688.

(107) Min, W.; Cheng, J.-X.; Ozeki, Y. Theory, innovations and applications of stimulated Raman scattering microscopy. *Nat. Photonics* **2025**, *19* (8), 803−816.